

DRAG COEFFICIENTS OF LONG FLEXIBLE CYLINDERS

SUBJECT TO VORTEX INDUCED OSCILLATIONS

by

James Carl McGlothlin

B.S., Texas A&M University
1980Submitted in Partial Fulfillment of the
Requirements for the Degree of

MASTER OF SCIENCE

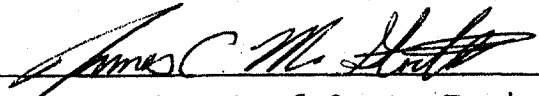
IN OCEAN ENGINEERING

at the

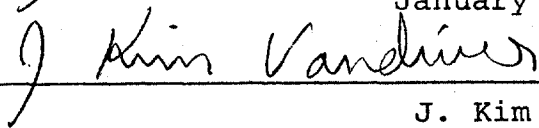
Massachusetts Institute of Technology

January, 1982

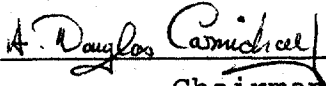
Signature of Author


Department of Ocean Engineering
January 29, 1982

Certified by


J. Kim Vandiver
Thesis Supervisor

Accepted by


Chairman, Department Committee

DRAG COEFFICIENTS OF LONG FLEXIBLE CYLINDERS

SUBJECT TO VORTEX INDUCED OSCILLATIONS

by

JAMES CARL MCGLOTHLIN

Submitted to the Department of Ocean Engineering
on January 28, 1982 in partial fulfillment of the
requirements for the Degree of Master of Science in
Ocean Engineering

ABSTRACT

Field tests were conducted to measure the drag force on long flexible cylinders subject to vortex-induced oscillations. Four different types of cylinders, each 75.0 feet long, were used in the experiments. These cylinders included a uniform cable, a cable with lumped masses, a cable with a vibration suppression fairing, and a steel tube. Flow velocities ranged from 0 to 2.4 feet/second. Drag force, current, and the horizontal and vertical acceleration of the cylinder at seven locations were simultaneously recorded. In addition, the tension on the cylinder was constantly monitored. From the data taken, drag coefficients and the horizontal and vertical RMS displacements of the cylinders were calculated. The drag coefficients for the vibrating flexible cylinders are much greater than their stationary values and show a strong dependence on the amplitude of vibration of the cylinder. A method for predicting the drag coefficient on a vibrating cylinder is used in several cases to compare with the measured values.

ACKNOWLEDGEMENTS

This research was part of a joint industry and government sponsored project supported by the American Bureau of Shipping, Brown and Root, Inc., Chevron Oil Field Research, Conoco, Inc., Exxon Production Research, Shell Development Company, Union Oil Research, the Office of Naval Research, and the U.S. Geological Survey.

An eight member team led by Professor J. Kim Vandiver participated in the field experiments. Prof. Vandiver was assisted during these experiments by Charles Mazel, Jen-Yi Jong, Ed Moas, Peter Stein, Mark Whitney, Pam Vandiver, and myself.

Prof. Vandiver also served as my thesis supervisor and his patience and guidance during my stay at M.I.T. was invaluable.

Finally, I would like to thank Anna Markowitz for typing this thesis and Bill McLaren for proofreading it.

TABLE OF CONTENTS

	<u>PAGE</u>
Abstract	3
Acknowledgements	4
Table of Contents	5
List of Figures	7
List of Symbols	10
Chapter I INTRODUCTION	12
Chapter II BACKGROUND THEORY	14
2.1 Basic Vortex Shedding Theory	14
2.2 Natural Frequencies and Mode Shapes	17
2.2.1 Cable	17
2.2.2 Steel Tubing	18
2.3 Drag Coefficients	18
Chapter III THE EXPERIMENT	24
3.1 Test Site	24
3.2 Drag Measuring System	26
3.3 Current Measuring System	29
3.4 Tension Measuring System	29
3.5 Test Cylinders	31
3.5.1 Cable	31
3.5.2 Steel Tubing	33
3.5.3 Lumped Masses	34
3.5.4 Faired Cable	35
3.6 Data Recording Equipment	35
Chapter IV DATA REDUCTION PROCEDURES	36
4.1 Drag and Current Data	36
4.2 Accelerometer Data	36

TABLE OF CONTENTS

(continued)

	<u>PAGE</u>
Chapter V RESULTS	46
5.1 2 1/2 Hour Drag Coefficient Records	46
5.2 Drag Coefficients at Lock-In	54
5.3 Non Lock-In Drag Coefficients	64
5.4 Predicted Drag Coefficients	67
Chapter VI CONCLUSIONS	69
References	77
APPENDIX	
A. Integration of Equation 2.11	79
B. Errors in the Drag Coefficient Calculations	81
C. Mechanical Properties and Dimensions of Test Cylinders and Lumped Masses	83
D. Drag Coefficients for Cables with Attached Lumped Masses	85

LIST OF FIGURES

<u>FIGURE</u>		<u>PAGE</u>
1	Uniform Flow Around a Stationary Cylinder	15
2	Drag Coefficient vs. Reynolds Number for a Smooth Stationary Cylinder	20
3	Mean In-Line Drag Coefficient of a Rigid Cylinder vs. d/VT for $A/d=0.25, 0.50, 0.75$, and 0.84 [13].	21
4	Experiment Site	25
5	Schematic Diagram of the Experiment Test Section	27
6	Diagram of the Drag Measuring Device	28
7	Schematic Diagram of the Tension Measuring Device	30
8	Cross Section and Side View of the Composite Cable	32
9	Raw Vertical Acceleration Signal	40
10	Acceleration Signal After Initial Least-Square Fit	41
11	Velocity Signal Before High-Pass Filter	42
12	Velocity Signal After High-Pass Filter	43
13	Displacement Signal Before Final Least-Square Fit	44
14	Displacement Signal After the Final Least-Square Fit	45
15	2 1/2 Hour Drag Coefficient Record for the Steel Tubing	47
16	Drag Coefficient Error Bounds for the 2 1/2 Hour Steel Tubing Record	48
17	2 1/2 Hour Drag Coefficient Record for the Bare Cable	49
18	Drag Coefficient Error Bounds for the 2 1/2 Hour Bare Cable Record	50

LIST OF FIGURES

(continued)

<u>FIGURE</u>		<u>PAGE</u>
19	2 1/2 Hour Drag Coefficient Record for the Faired Cable	51
20	Drag Coefficient Error Bounds for the 2 1/2 Hour Faired Cable Record	52
21	Vertical Displacement Time History of the Steel Tubing at Lock-In	55
22	Lock-In Motion of the Steel Tubing at Position L/6	56
23	FFT of the Steel Tubing at Lock-In	58
24	FFT of the Bare Cable at Lock-In	59
25	Drag Coefficient Record of the Steel Tubing During Third Mode Vertical and Fifth Mode Horizontal Response	60
26	Drag Coefficient Record of the Steel Tubing Changing from Third Mode Vertical and Fifth Mode Horizontal Response to Random Response	61
27	Drag Coefficient Record of the Steel Tubing Changing from Second Mode Vertical and Third Mode Horizontal Response to Random Response	62
28	Drag Coefficient Record of the Bare Cable During Third Mode Vertical and Fifth Mode Horizontal Response	63
29	Non Lock-In Vertical Displacement Time History of the Steel Tubing	65
30	Non Lock-In Motion of the Steel Tubing at Position L/6.	66
31	Non Lock-In FFT of the Steel Tubing	71
32	Non Lock-In FFT of the Bare Cable	72
33	Drag Coefficient Record of the Steel Tubing During Non Lock-In Response	73

LIST OF SYMBOLS

a	Local vertical displacement (in.)
A	Modal amplitude of vibration for a flexible cylinder and vertical amplitude of vibration for a rigid cylinder (in.)
C_D	Drag coefficient calculated from the experiment data.
C_{DL}	Predicted local drag coefficient
C_{DL}	Lower error bound on the calculated drag coefficient
C_{DO}	Drag coefficient for a stationary cylinder.
C_{DT}	Predicted average drag coefficient for a flexible vibrating cylinder.
C_{DU}	Upper error bound on the calculated drag coefficient
d	Cylinder diameter (in.)
D	Measured drag force on the flexible vibrating cylinders (lbs.)
f_n	Cylinder natural frequency (Hz)
f_s	Frequency at which vortex pairs are shed (Hz)
g	Acceleration of gravity (in/s ²)
L	Length of cylinder (ft.)
m	Mass per unit length of test cylinders (slugs/ft.)
n	Mode number
P	Tension (lbs.)
ρ	Density of fluid (slugs/ft. ³)
S	Projected area of the cylinder normal to the direction of flow (ft. ²)
St	Strouhal number

LIST OF SYMBOLS
(continued)

T	Period of transverse oscillation (s)
V	Velocity of flow (ft/s)
V_r	Reduced velocity
W_r	Wake parameter
y	Mode shape of the pinned-pinned flexible cylinder

CHAPTER I
INTRODUCTION

Vortex shedding from a cylindrical shaped object is a result of flow separation. These shed vortices cause unsteady forces to be imposed on the cylinder by varying the local pressure distribution. If the cylinder is able to respond to these unsteady forces, motion may result in both the transverse and in-line direction. In addition to the reduced fatigue life due to this motion, the transverse oscillations cause an increase in the steady drag force that may greatly exceed the design limits. Marine drilling risers, hydrophone cables, and deep water moorings used to anchor floating platforms are all examples of cylinders in the marine environment that may experience vortex induced oscillations.

The purpose of the research work presented here was to determine the drag forces on a long flexible cylinder that was excited by vortex shedding. To accomplish this, a series of field tests were performed during the summer of 1981. In the tests, 75 foot long cylinders were placed between supports on a sandbar that was exposed at low tide and submerged at high tide. During these tide changes, the current caused vortices to be shed from the cylinders and as a result the cylinders were excited. Measurements taken during this time included the drag force on the cylinder, cylinder tension, current, and the horizontal and vertical acceleration

of the cylinder at seven locations along its length.

Two basic types of cylinders were used in the tests. First, a composite cylinder with negligible bending rigidity was designed specifically for the tests to house seven accelerometer pairs and to act as a model for a cable. Second, steel tubing was used as a model for a marine riser. The steel tubing had a slightly larger I.D. than the cable's O.D. so the cable could be placed inside the steel tubing. In this way, the response of the steel tubing could be measured by the accelerometers in the cable. In addition to the tests run on these two cylinders, tests were also performed using the cable with either fairings or lumped masses attached to it. However, only a limited amount of data will be presented on the faired cable and on the cable with lumped masses.

The drag force data is presented in terms of the drag coefficient and is plotted alongside the current and RMS displacement of the cylinder. In addition, results from a method for predicting the drag coefficient for an oscillating cylinder will be compared to measured results.

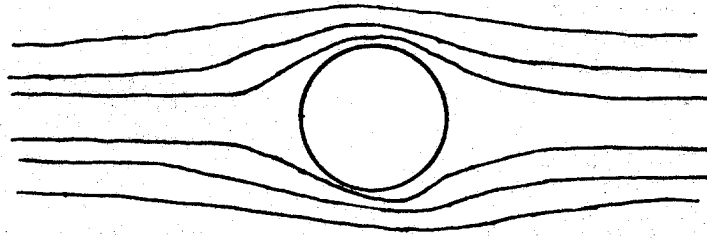
CHAPTER II

BACKGROUND THEORY

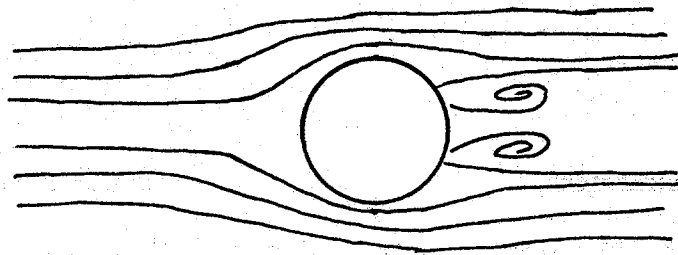
2.1 Basic Vortex Shedding Theory

When a stationary rigid cylinder is placed in a steady current with its axis normal to the direction of the flow, vortices are shed as a result of flow separation. This vortex shedding process is described best by its relation to the Reynolds number. At Reynolds numbers less than 1, the flow around a stationary cylinder is uniform with no vortices being shed. The flow resembles that of an ideal fluid where viscous effects have been neglected [Figure 1a]. As the Reynolds number is increased, vortices begin to shed symmetrically from the cylinder [Figure 1b]. This symmetric shedding will continue up to Reynolds numbers around 40. At this point, instabilities begin to develop in the wake region and the vortices start to shed in an alternating fashion [Figure 1c].

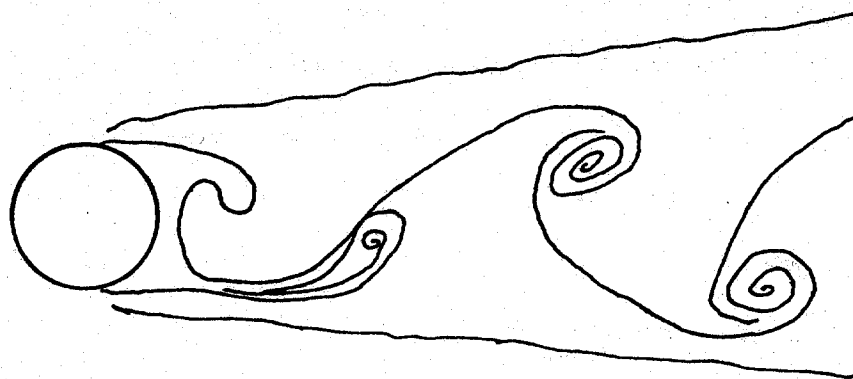
As a result of these vortices being shed, forces are imposed on the cylinder. In the flow direction, in addition to a steady drag force, there is also a fluctuating drag force associated with the individual shedding of vortices. If the Reynolds number is above 40, an alternating lift force will also be present. This alternating lift force is a result of the transverse pressure gradient set up by the non-symmetric shedding of vortices and acts in a direction away from the last detached vortex [14]. The lift force frequency



a) Reynolds number less than 1



b) Reynolds number between 1 and 40



c) Reynolds number greater than 40

Figure 1. Uniform Flow Around a Stationary Cylinder

is equal to the frequency at which pairs of vortices are shed while the fluctuating drag force frequency is twice this since it is associated with individual shedding of vortices.

The Strouhal number, $St = f_s d/V$, is a non-dimensional number which relates the frequency at which pairs of vortices are shed (f_s) and the diameter of the cylinder (d) to the flow velocity (V). The Strouhal number is a function of the Reynolds number. However, over a wide range of Reynolds numbers (100 to 10^5) the Strouhal number for a smooth stationary cylinder is nearly constant and equal to about .2 [10].

If the cylinder is flexible or flexibly mounted and lightly damped, the fluctuating forces cause oscillations to occur in both the in-line and transverse direction. The oscillations in the transverse direction will dominate with amplitudes generally believed to be an order of magnitude greater than those in the in-line direction. These oscillations cause lift and drag forces to increase and also result in a reduction in the shedding frequency. If the vortex shedding frequency is within a range of about $\pm 25\%$ of one of the natural frequencies of the cylinder, a phenomena known as lock-in can occur [14]. When lock-in occurs, the vortex shedding frequency moves to the frequency of oscillation of the cylinder in a violation of the Strouhal relationship. Lock-in causes a resonant excitation of the cylinder with corresponding increases in response amplitude and drag. This lock-in condition will continue until the predicted vortex shedding frequency is out of the $\pm 25\%$ range. At this time

the vortex shedding frequency will jump to a frequency close to that predicted by the Strouhal relationship.

2.2 Natural Frequencies and Mode Shapes

2.2.1 Cable

A cable with negligible bending rigidity can be modeled as an ideal string. The differential equation governing the motion of the cable as given by the ideal string equation is:

$$\left(\frac{P}{m}\right) \frac{d^2 y}{dx^2} = \frac{d^2 y}{dt^2} \quad (2.1)$$

where: P = Tension

m = Mass per unit length of the cylinder.

If the cable is vibrating in water, added mass effects must be considered. The theoretical added mass coefficient for a stationary cylinder is 1.0. However, the added mass coefficient for a vibrating cylinder may be less than 1.0.

Solution of this differential equation leads to the following expressions for the natural frequencies of the cable:

$$f_n (\text{Hz}) = \left(\frac{n\pi}{L}\right) \sqrt{\frac{P}{m}} \quad (2.2)$$

where: n = Mode number

L = Length of the cylinder

The mode shapes for the ideal string are simple sinusoids given by:

$$y = A \sin\left(\frac{n\pi x}{L}\right) \quad (2.3)$$

where: A = The modal response amplitude.

A limited number of tests were conducted on a cable with fairings. The natural frequencies of the cable with fairings will be somewhat lower due to the additional mass and added mass of the fairings. However, no formal analysis of the faired cables dynamic behavior will be presented.

2.2.2 Steel Tubing

Since the steel tubing used in the experiments had a bending rigidity that cannot be neglected, it is not possible to model it as an ideal string. Instead, a good model for the steel tubing is a beam under tension with pinned ends. The natural frequencies for a beam under tension are given by [2]:

$$f_n \text{ (Hz)} = \frac{\lambda_n^2}{2\pi L^2} \sqrt{\frac{EI}{m}} \quad (2.4)$$

where:

$$\lambda_n^2 = n^2 \pi^2 \sqrt{1 + \frac{PL^2}{EI n^2 \pi^2}} \quad (2.5)$$

and EI is the bending rigidity of the cylinder.

The effects of rigidity on the natural frequencies of the steel tubing become more prevalent at the higher mode numbers. In addition, the rigidity causes the modal frequencies to be spaced further apart than the corresponding cable values. The mode shapes for a beam under tension are exactly the same as those for the cable.

2.3 Drag Coefficients

For a smooth cylinder in a steady flow, the dominant contribution to the drag force is due to separation.

Separation causes an area of reduced pressure to form in the wake of the cylinder. This substantial pressure difference between the forebody and afterbody of the cylinder results in a net force being applied to the cylinder in the flow direction. The expression for the mean drag force on a cylinder is given by:

$$D = \frac{1}{2} C_D \rho S V^2 \quad (2.6)$$

where: C_D = Drag coefficient

ρ = Density of the fluid

S = Projected area normal to the direction of the flow.

For smooth stationary cylinders, there is a great deal of experimental data relating drag coefficient to Reynolds number. An example is shown in Figure 2 [8, 15]. However, if the cylinder is allowed to respond dynamically to the vortex shedding forces this relationship is no longer valid.

The drag force on a vibrating rigid cylinder is not only a function of flow speed but also the amplitude of vibration of the cylinder. The drag force increases with amplitude because the cylinder presents a larger apparent projected area to the flow. This force peaks when the cylinder is locked-in and responding resonantly. Sarpakaya [13] has performed tests in recirculating water tunnels using short rigid aluminum tubes. The results from these tests are shown in Figure 3. The data in the figure was taken at flow speeds of .84 and 1.3 ft/s with cylinder diameters of .7 and 1.0 inches. In Sarpakaya's tests, the cylinder was sinusoidally driven

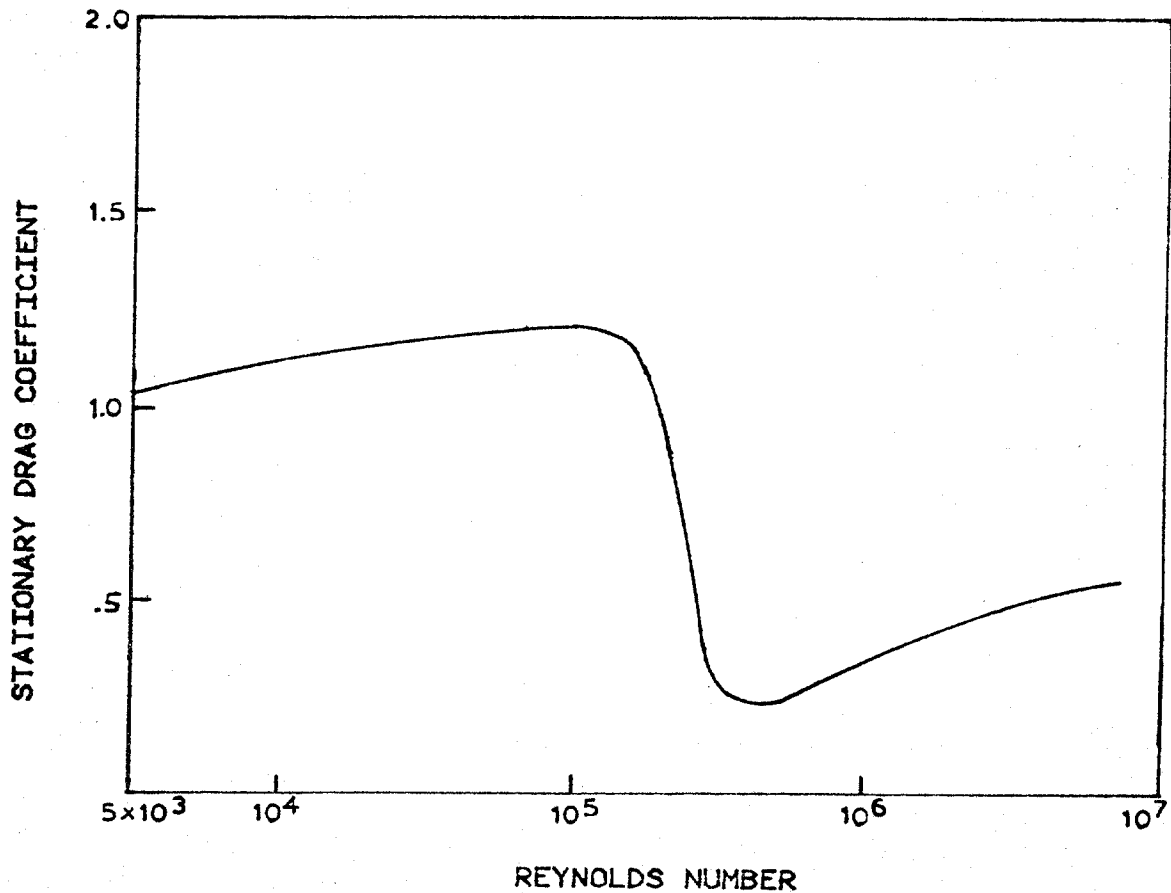


FIGURE 2. DRAG COEFFICIENT VS. REYNOLDS NUMBER FOR A SMOOTH STATIONARY CYLINDER.

and the drag force was measured directly. The drag coefficient results show a distinct dependence on the amplitude to diameter ratio A/d . In addition, the drag coefficients are also affected by the period of oscillation T . Sarpakaya uses the non-dimensional parameter d/VT and the data shows a peak at values between .18 and .20.

Griffin and Ramberg [7] also measured the drag forces on a vibrating rigid cylinder. Their technique for measuring the drag force involved measuring various wake parameters and applying the von Karman drag formulation. The data was taken at a Reynolds number of 144 and their results show that vib-

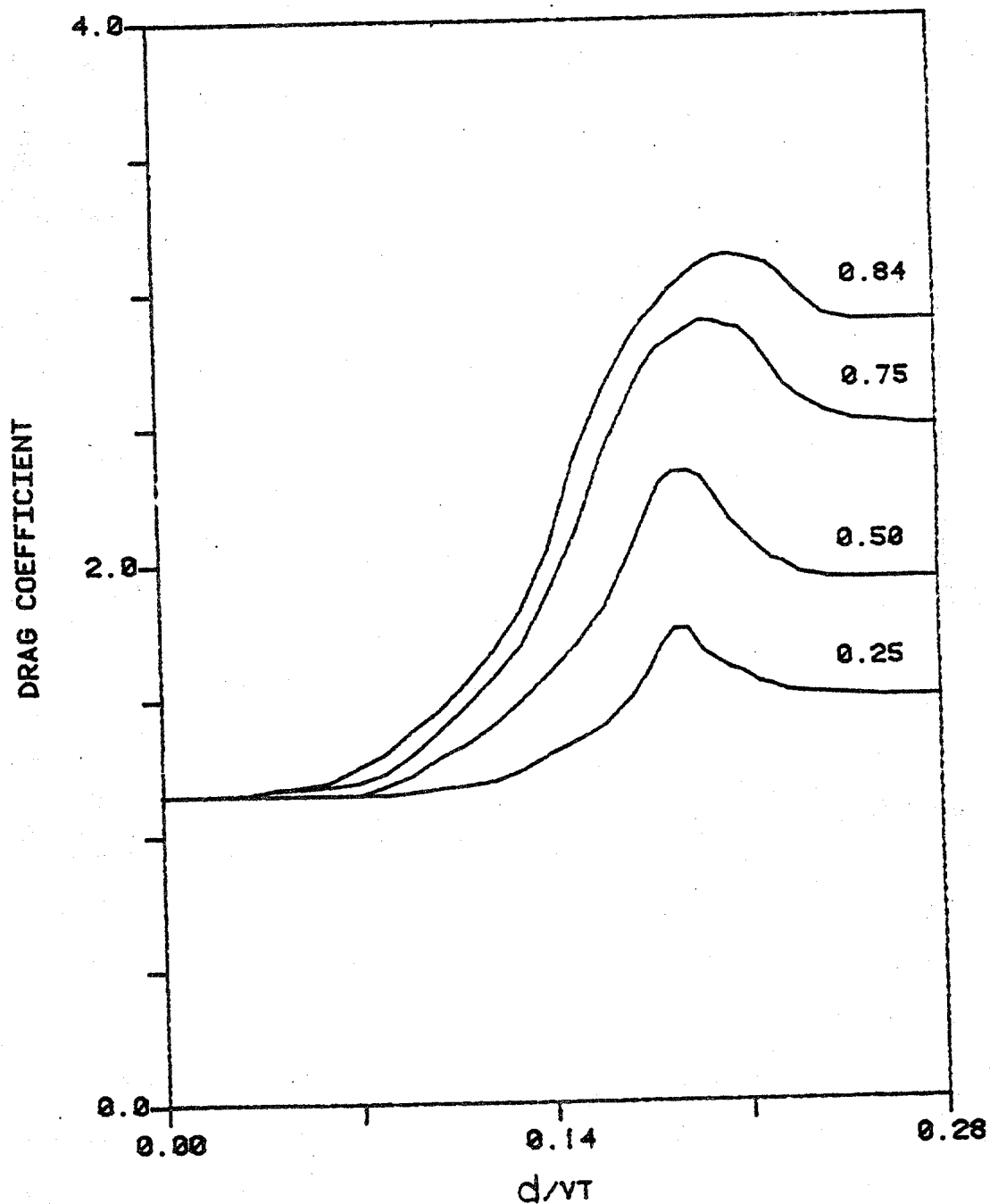


FIGURE 3. MEAN IN-LINE DRAG COEFF. OF A RIGID CYLINDER VS. d/vt FOR $A/d = 0.25, 0.50, 0.75, \text{ AND } 0.84.$ [13]

ration can cause an increase of up to 184 percent in the stationary drag coefficient.

When a cylinder is flexible and placed in a flow, the flow can excite the cylinder to respond in both the in-line and transverse directions. This response causes increases in drag and makes the force mechanism even more difficult to understand because the in-line response couples with the transverse response to affect the magnitude and path of the cylinder motion. Thus, the drag forces on the flexible cylinder are functions not only of current, density, and projected area but also response frequency, modal amplitude and mode shape.

Skop, Griffin and Ramberg [17] did a least-squares fit of data taken from the SEACON II project and derived the following empirical expression for the local drag coefficient as a function of the amplitude and frequency of vibration of a cylinder:

$$C_{D1}/C_{D0} = 1 + 1.16(W_r - 1)^{.65} \quad (2.7)$$

where: C_{D0} = Drag coefficient for a stationary cylinder

W_r = Wake stability parameter.

The wake stability parameter contains the important dynamic properties of the cylinder and is given by:

$$W_r = (1 + 2a/d)(StV_r)^{-1} \quad (2.8)$$

where: a = Local vibration amplitude

V_r = Reduced velocity ($V/f_n d$)

Substituting values into the wake stability parameter for

St and V_r gives:

$$W_r = (1+2a/d) (f_n/f_s) \quad (2.9)$$

Furthermore, if we confine ourselves to cases at lock-in we can reduce W_r to:

$$W_r = (1+2a/d) \quad (2.10)$$

The expression for the local drag coefficient for a vibrating cylinder then becomes:

$$C_{Dl}/C_{DO} = 1+1.16(2a/d)^{.65} \quad (2.11)$$

To find the average drag coefficient for the vibrating flexible cylinder, we must replace the local amplitude with the mode shape, integrate over the length of the cylinder and then divide by the length. Using the mode shape given in Equation 2.3, the above equation can be numerically integrated [Appendix A] to give the following expression for the drag coefficient of a vibration flexible cylinder:

$$C_{DT} = C_{DO} [1+.833 \left(\frac{2A}{d}\right)^{.65}] \quad (2.13)$$

where A is the modal amplitude. By limiting ourselves to cases at lock-in where the mode shapes and shedding frequency are known, the drag coefficient relationship has been reduced to one which depends only upon the modal amplitude.

CHAPTER III
THE EXPERIMENT

3.1 Test Site

The site chosen for the experiment, shown in Figure 4, was a sandbar located at the mouth of Holbrook Cove near Castine, Maine. This was the same site used in previous experiments in 1975 and 1976 by Vandiver, Mazel and Kan [12, 18]. At low tide, the sandbar was exposed allowing easy access to the test equipment while at high tide it was covered by about 10 feet of water. The test section was oriented normal to the direction of the current which varied from 0 to 2.4 ft/s over the tidal cycle with only small spatial differences over the section length at any given moment.

The data taking station for the experiment was the R/V Edgerton chartered from the MIT Sea Grant Program. The Edgerton was moored for the duration of the experiment approximately 300 feet from the sandbar and connected to the instruments on the sandbar by umbilicals.

Prior to the data taking part of the experiment, a few days were needed to prepare the site. A foundation for the experiment was needed to anchor the supports that were to hold the ends of the test cylinders. To accomplish this, six 4.5 inch diameter steel pipes were water jetted into the sandbar utilizing the fire pump aboard the Edgerton. These six pipes were made of two five foot sections joined by

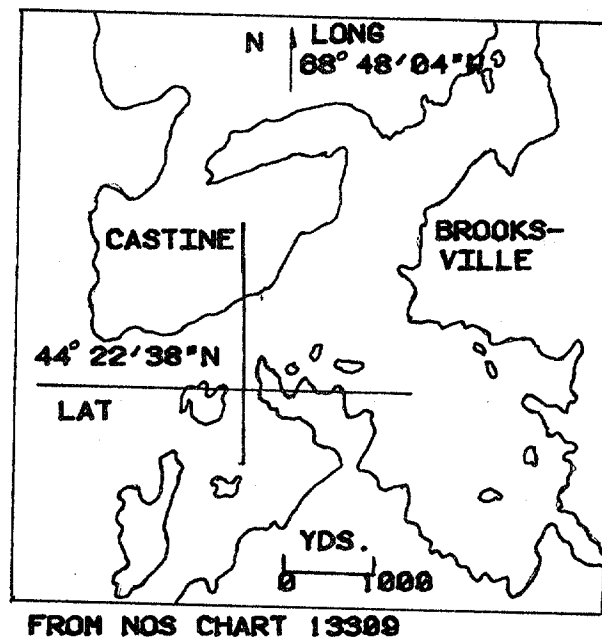
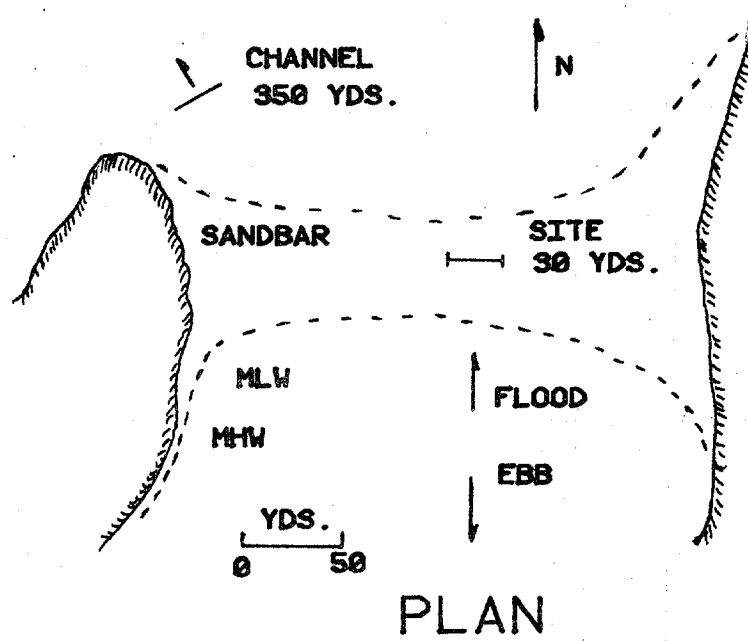


FIGURE 4. EXPERIMENT SITE

couplings so that the overall length of each was 10.0 feet. In addition, one 2.0 inch steel pipe 6 feet long was jetted into the sandbar to be used as a current meter mount. Finally, a section of angle iron was clamped to the pipe used to support the drag measuring mechanism and attached to another support pipe to prevent any rotation of the drag mechanism mount. Figure 5 shows a schematic diagram of the experiment test section.

3.2 Drag Measuring System

The drag measuring mechanism was located at the west end of the experiment test section. A 3 foot pipe was coupled to the inner support pipe. Onto this short pipe the drag mechanism was welded 2.5 feet above the mudline. The outer two support pipes were guyed to this short pipe to prevent any creep when the system was under load. The drag measuring mechanism [Figure 6] consisted of a .25 inch stainless steel triangular plate that was welded to a 1.0 inch stainless steel shaft. The shaft was supported by a pillow block bearing at either end. These bearings were bolted through 1.0 inch spacers to a 15.25 x 8.0 x .25 inch steel plate which was welded to the 3 foot pipe section. Along the backside of the triangular plate, a 1.0 inch piece of angle iron was attached to serve as a contact point for a Sensotec Model 41 load cell. The test cylinders were pin connected to the triangular plate at the forward corner. The drag mechanism was designed so that a drag force applied by the test cylinder at the pin would generate a moment about the 1.0 inch shaft. This moment

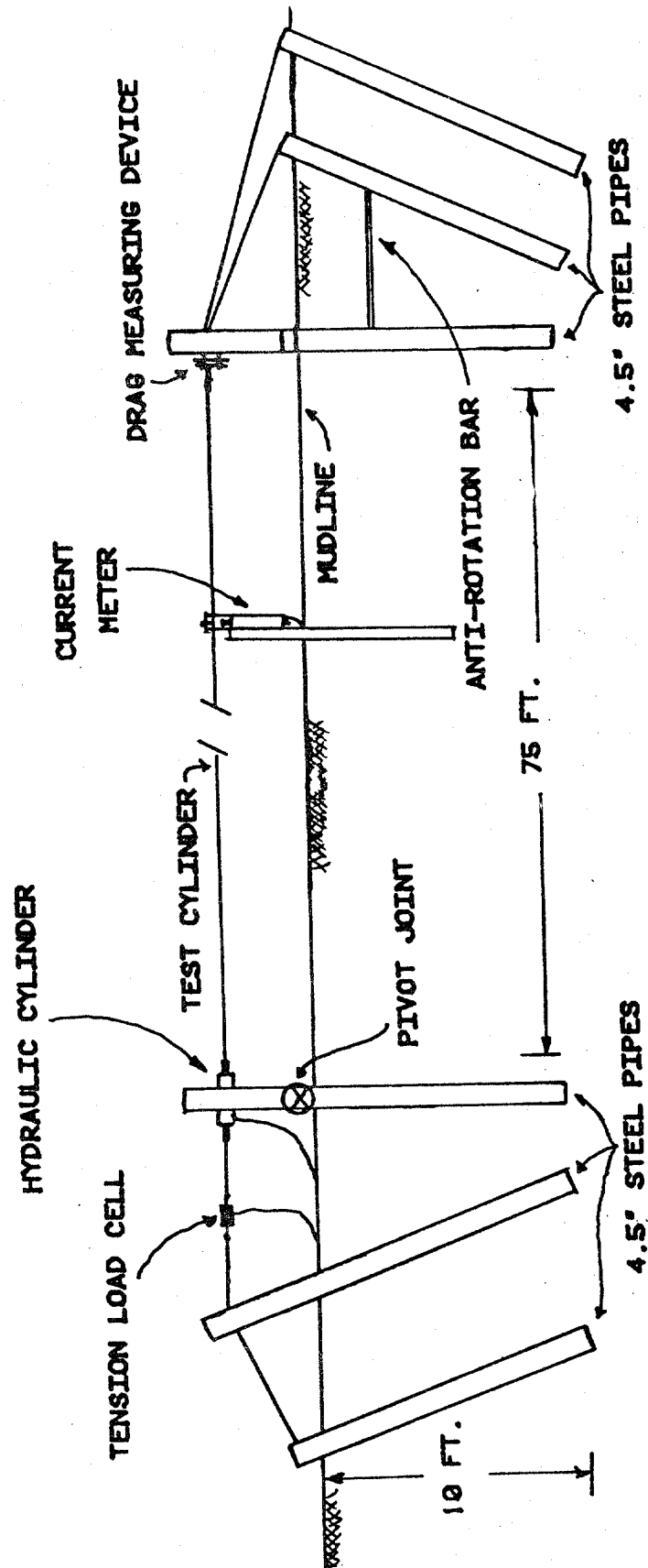
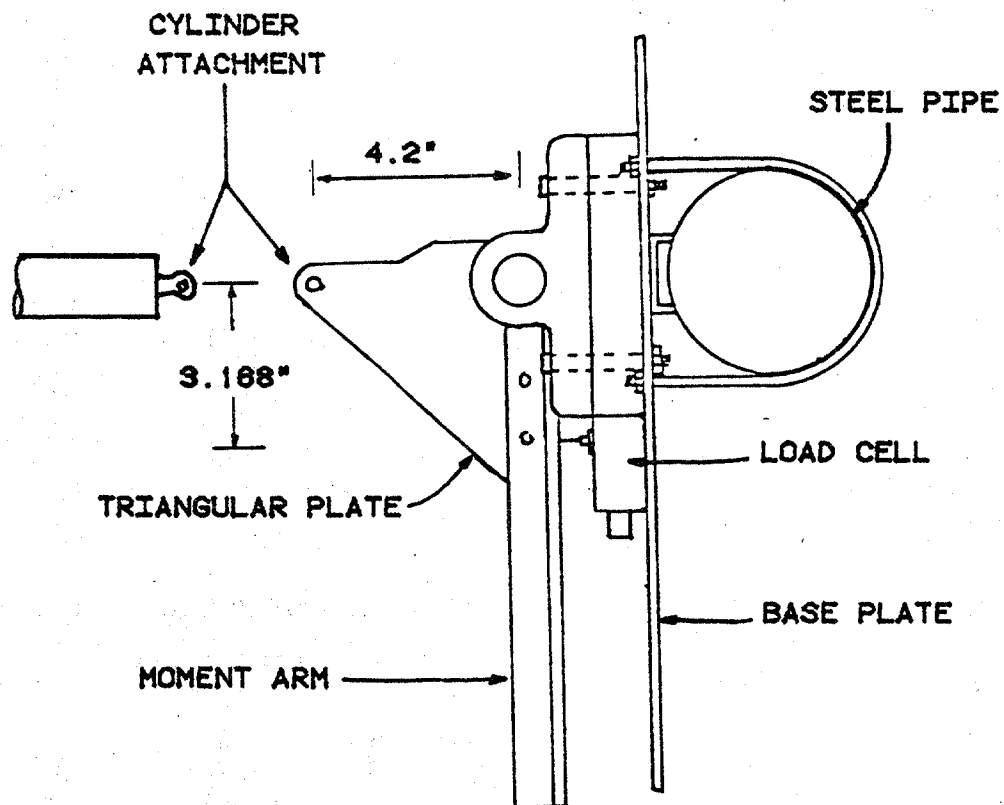
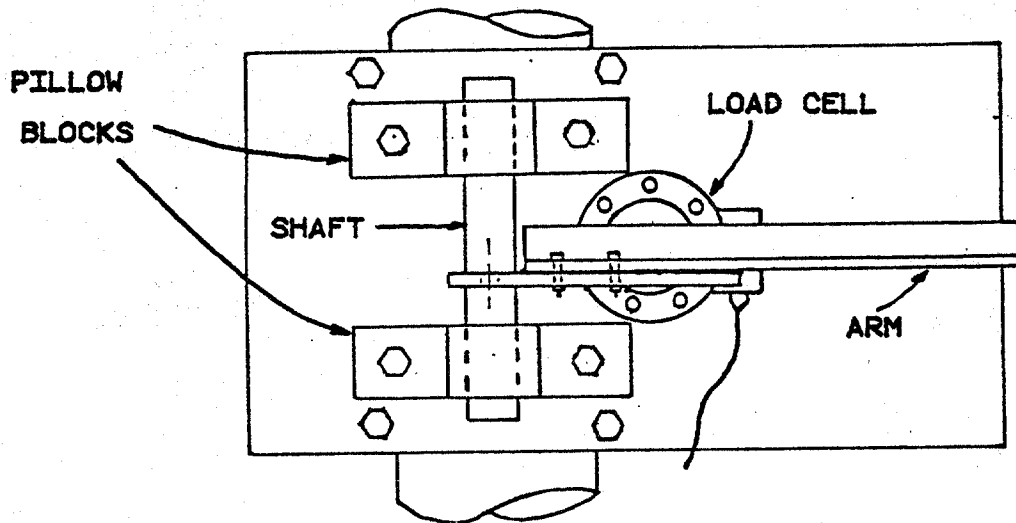


FIGURE 5. SCHEMATIC DIAGRAM OF THE EXPERIMENT TEST SECTION



TOP VIEW



FRONT VIEW

FIGURE 6. DIAGRAM OF THE DRAG MEASURING DEVICE

would be in equilibrium with the moment generated by the force on the load cell. The load cell could be moved to different locations to obtain the most favorable moment arm ratio. The signal from the load cell traveled through wires in the test cylinder and through the umbilicals to the Edgerton where they were conditioned and recorded.

3.3 Current Measuring System

The current was measured by a Neil Brown Instrument Systems DRCM-2 Acoustic Current Meter located 12.5 feet from the west end of the test cylinder and 2 feet upstream. It was set so that it determined the current at the level of the test cylinders. Signals from the current meter traveled through umbilicals to the Edgerton where they were monitored and recorded. In addition, a current meter traverse was performed using an Endeco current meter to determine the spatial differences in current along the test section. The current was found to be spatially uniform to within $\pm 3.0\%$ from end to end for all but the very low current speeds ($V < 0.5$ ft/s).

3.4 Tension Measuring System

The tension measuring and adjusting system [Figure 7] was located at the east end of the experiment test section. Extensions were made to the two inner water jetted posts at this end. As shown in the diagram, a 5 foot extension was made to the center post and a 3 foot extension was made to the inner most post. What made this 3 foot extension different from the rest was that its attachment to the jetted pipe

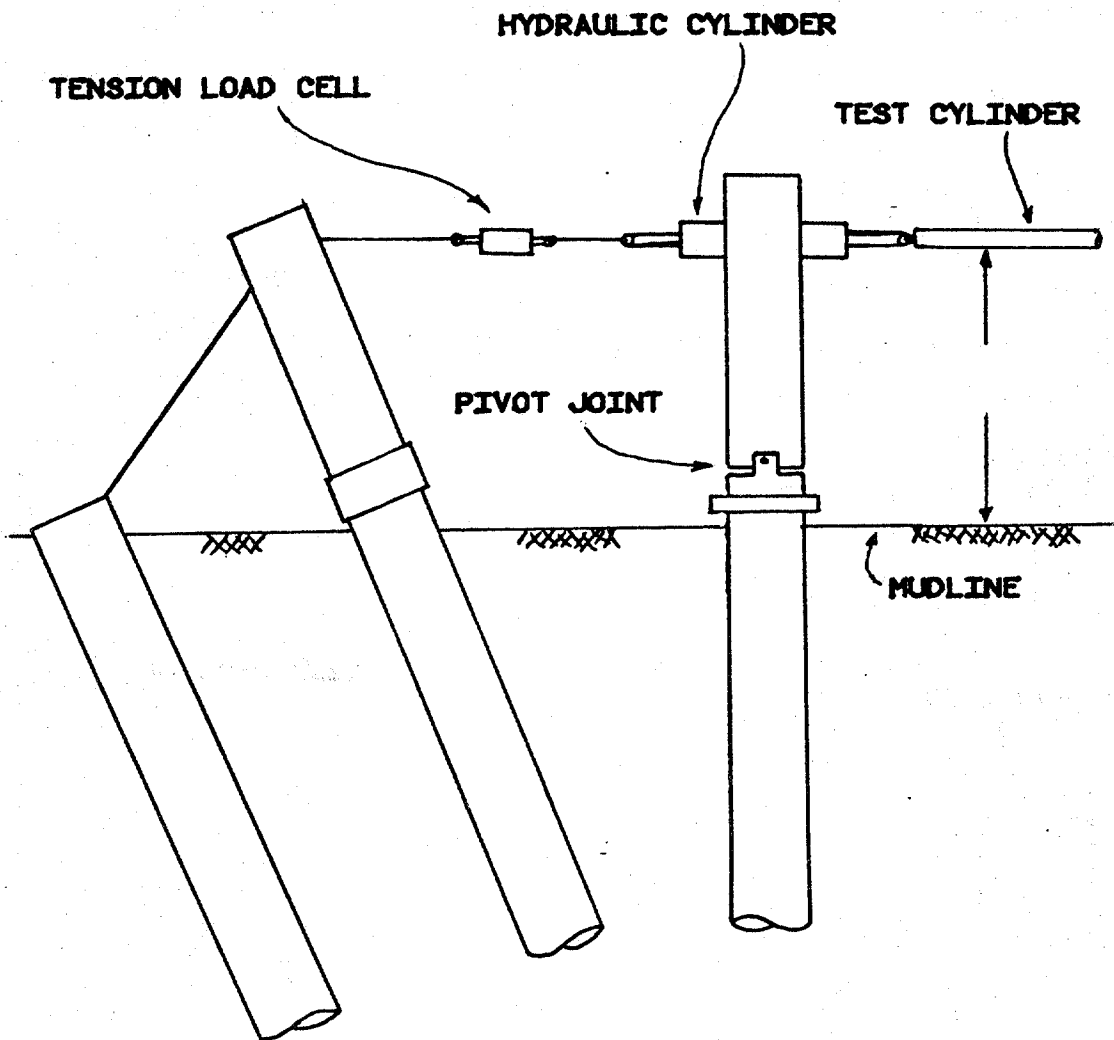


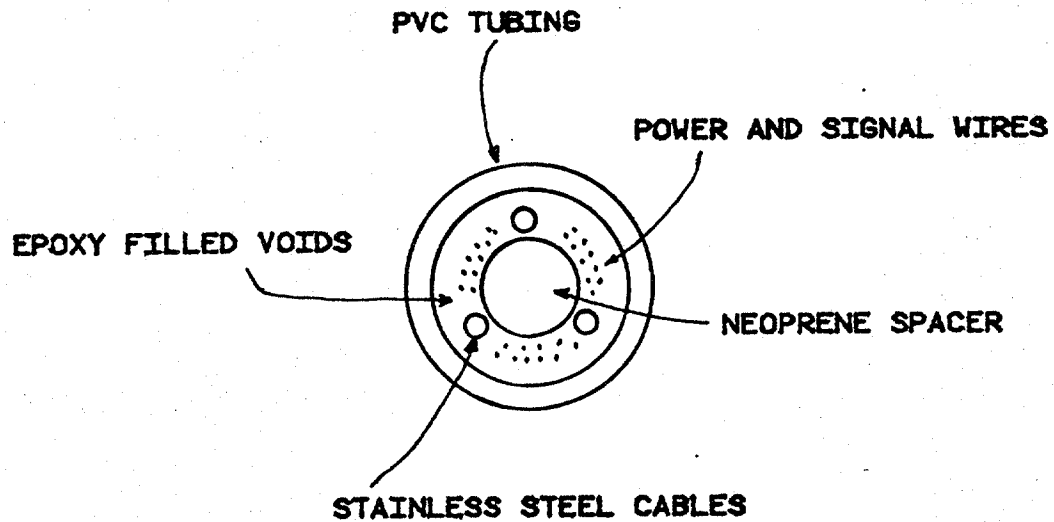
FIGURE 7. SCHEMATIC DIAGRAM OF THE
TENSION MEASURING SYSTEM

at the mudline was a pin connection as compared to the standard pipe couplings used on the other extensions. This pin connection gave it the ability to pivot in the plane of the posts. Onto this pivoting post, a hydraulic cylinder was mounted 2.5 feet above the mudline. The test cylinders used in the experiments were connected at one end to this hydraulic cylinder and at the other end to the drag measuring device. The test cylinders were attached 2.5 feet above the mudline, a sufficient distance to avoid any boundary layer effects caused by the sandbar. A cable ran from the back of the hydraulic cylinder to a Sensotec Model RM In-Line load cell which was anchored at the other end to the center post. In this way, the force on the test cylinders was the same force seen by the load cell minus a small amount of friction in the pin. The output from the tension load cell passed through the umbilicals to the Edgerton where it was monitored. Hydraulic hose ran from a hand operated pump on the Edgerton to the hydraulic cylinder so that the tension could be changed as desired.

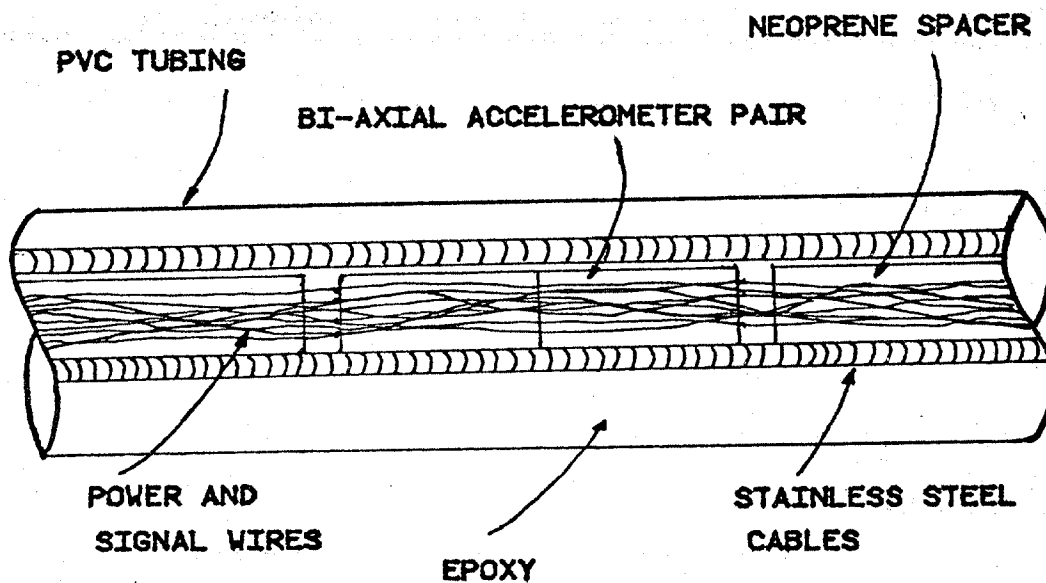
3.5 Test Cylinders

3.5.1 Cable

A 75 foot long composite cable was developed specifically for the experiments that were performed in the summer of 1981. Figure 8 shows a cross-section and side view of the test cable. The outer sheath for this cable was a 75 foot long piece of clear flexible PVC tubing, which was 1 1/4 inches O.D. by 1.0 inch I.D. Three 1/8 inch stainless steel cables



CROSS SECTION



SIDE VIEW

FIGURE 8. CROSS SECTION AND SIDE VIEW
OF THE COMPOSITE CABLE

ran through the tubing and served as the tension carrying members. A cylindrical piece of 1/2 inch neoprene rubber was used to keep the stainless steel cables spaced 120 degrees apart. The neoprene rubber spacer was continuous along the length except at seven positions where biaxial pairs of accelerometers were placed. Starting at the east end, these positions were at $L/8$, $L/6$, $L/4$, $2L/5$, $5L/8$, and $3L/4$. These accelerometers were used to measure the response of the cable as the shed vortices excited it. The accelerometers were Sundstrand Mini-Pal Model 2180 Servo Accelerometers which were sensitive to the direction of gravity. The biaxial pairing of these accelerometers made it possible to determine their orientation and hence extract real vertical and horizontal accelerations of the cable at the seven locations. Three bundles of ten wires each ran along the sides of the neoprene spacer to provide power and signal connections to the accelerometers and also to provide power and signal connections to the drag measuring system. Finally, an Emerson and Cuming flexible epoxy was used to fill the voids in the cable and make it watertight. The weight per unit length of this composite cable was .7704 lbs/ft.

3.5.2 Steel Tubing

In a second set of experiments, the composite cable was placed inside a 1.631 inch O.D. by 1.493 inch I.D. steel tubing so that stiffness effect could be studied. The tubing was made of four equal sections that were joined together to be the same length as the cable. The tubing was connected

to the hydraulic cylinder and to the drag cell mechanism by special connectors. At the internal joints steel nipples were welded to each end and stainless steel couplings were used to join them. The special end connectors kept the cable inside the tubing under a slight tension and neoprene spacers at intervals of 18 inches between the cable and tubing inhibited any relative motion between the two. The remaining cavity was allowed to fill with water. The weight per unit length of the steel tubing with the cable inside and the voids flooded with water was 2.2344 lbs/ft.

3.5.3 Lumped Masses

In another set of experiments, lumped masses were fastened to the bare cable and their effects studied. The lumped masses were made of cylindrical PVC stock each 12.0 inches long with a 3.5 inch diameter. A 1.25 inch hole was drilled through the center of each lumped mass so that the cable could pass through. In addition, four .625 inch holes were drilled symmetrically around this 1.25 inch center hole so that copper tubes filled with lead could be inserted to change the mass of the lumps. In the field, it was difficult to force the cable through the holes drilled in the PVC so the masses were cut in half along the length of their axis. The masses could then be placed on the cable in halves and held together by hose clamps. Different tests were run by varying the number and location of lumps and by changing the mass of the lumps. An example of these tests is reported on in Appendix D.

3.5.4 Faired Cable

Finally, $11.6 \times \frac{1}{16}$ inch diameter Endeco plastic stranded fairings were applied to the cable to see what effects they would have on the response amplitude and drag of the cable.

The mechanical properties and dimensions of the test cylinders and lumped masses and fairings are summarized in Appendix C.

3.6 Data Recording Equipment

During the experiment, data taken from the instruments on the sandbar was recorded in two ways. First, analog signals from the 14 accelerometers as well as current and drag were digitized, at 30.0 Hz per channel, onto floppy disks using a Digital Equipment MINC-23 Computer. Second, analog signals from the drag cell, current meter, and 6 accelerometers were recorded by a Hewlett-Packard 3968A Recorder onto 8-track tape. The floppies were limited to record lengths of 8 1/2 minutes and were used to take data at several times in each 2 1/2 hour data taking period. A Hewlett-Packard 3582A Spectrum Analyzer was set up to monitor the real time outputs of the accelerometers. The 8-track tape was used to provide a continuous record of the complete 2 1/2 hour data cycle.

CHAPTER IV

DATA REDUCTION PROCEDURES

4.1 Drag and Current Data

Drag and current data was taken to obtain the steady drag coefficients for the test cylinders. The drag data was block averaged to try to eliminate the high frequency effects associated with individual shedding of vortices. The current data was handled in a similar manner so that the drag coefficients could be calculated discretely using Equation 2.1. For the long records showing the drag coefficients over a 2 1/2 hour cycle, the average was taken over every 8.55 seconds of data and for the short records showing specific examples of the cylinders behavior the average was over every 2.33 seconds of data.

4.2 Accelerometer Data

Acceleration data taken from the seven biaxial pairs of accelerometers was used to find the horizontal and vertical RMS response of the test cylinder. The accelerometers were placed in biaxial pairs at seven locations along the test cylinder to give the best indication of modal response.

The initial step in dealing with the acceleration data was to find the real vertical and horizontal acceleration of the accelerometer pairs. The accelerometer pairs could not be set in the test cylinders with one exactly horizontal and the other exactly vertical, they were usually off by some

angle. The problem was to determine this angle and rotate the signals back to true horizontal and vertical accelerations. Each accelerometer used was sensitive to gravity and gave a DC offset that was a function of the angle its sensitive axis made to the direction of gravity. For the case where the sensitive axis was in the direction of gravity, the DC offset would be 1.0 volts, since the sensitivity was 1.0 volt/g, and if the sensitive axis was normal to the direction of gravity the DC offset would be 0. Since the accelerometers were fixed in biaxial pairs, the combination of the two DC offsets could be used to obtain the angle necessary to rotate the signals through to get true vertical and horizontal acceleration. Equation 4.1 shows the relation between the DC offsets and the rotation angle. In this case K is a constant whose value depends on which quadrant the accelerometer used to measure vertical acceleration was located.

$$\theta = \text{ARCTAN} \left[\frac{|\text{HORIZONTAL DC}|}{|\text{VERTICAL DC}|} \right] + K\pi \quad (4.1)$$

Once the true vertical and horizontal accelerations had been found, a double integration was performed on the data to obtain vertical and horizontal displacement. A seven step process was developed by Jen-Yi Jong of MIT to perform this double integration. The first step least-square fits the raw acceleration data to remove any linear trends that might be present. Second, an integration technique based on work done by Schuessler and Ibler [16] is applied to the data to give velocity. After this initial integration, a least-square fit

followed by a high-pass filter is applied to the velocity data to eliminate any low frequency noise that may have been expanded in the integration process. The integration-least-square fit-high-pass filter sequence is then repeated to give the displacements of the cylinder at each accelerometer pair. Figures 9 through 14 show an example of the integration process on a vertical acceleration signal.

The displacement data from the fourteen accelerometers was used to determine the vertical and horizontal mode shapes of the cylinder. This was done by filtering the displacement data from the fourteen accelerometers to the known theoretical mode shapes of the cylinders, using a least square technique.

The displacement data was also used to obtain the RMS response amplitude of the test cylinders at the location of the accelerometer pairs. The RMS expression is given in Equation 4.2. The summation period for the RMS data was the same as that used in the averaging of the drag and current data.

$$RMS = \sqrt{\frac{\sum_{i=1}^N (X_i)^2}{N}} \quad (4.2)$$

Finally, if the displacement data exhibited single mode response characteristics, the vertical RMS displacement data for an accelerometer location could be scaled to the modal amplitude and used in conjunction with Equation 2.12 to predict the steady drag coefficient for the oscillating cylinder. The stationary drag coefficient used in these predictions was

1.175 which corresponds to the typical Reynolds numbers seen in the experiments.

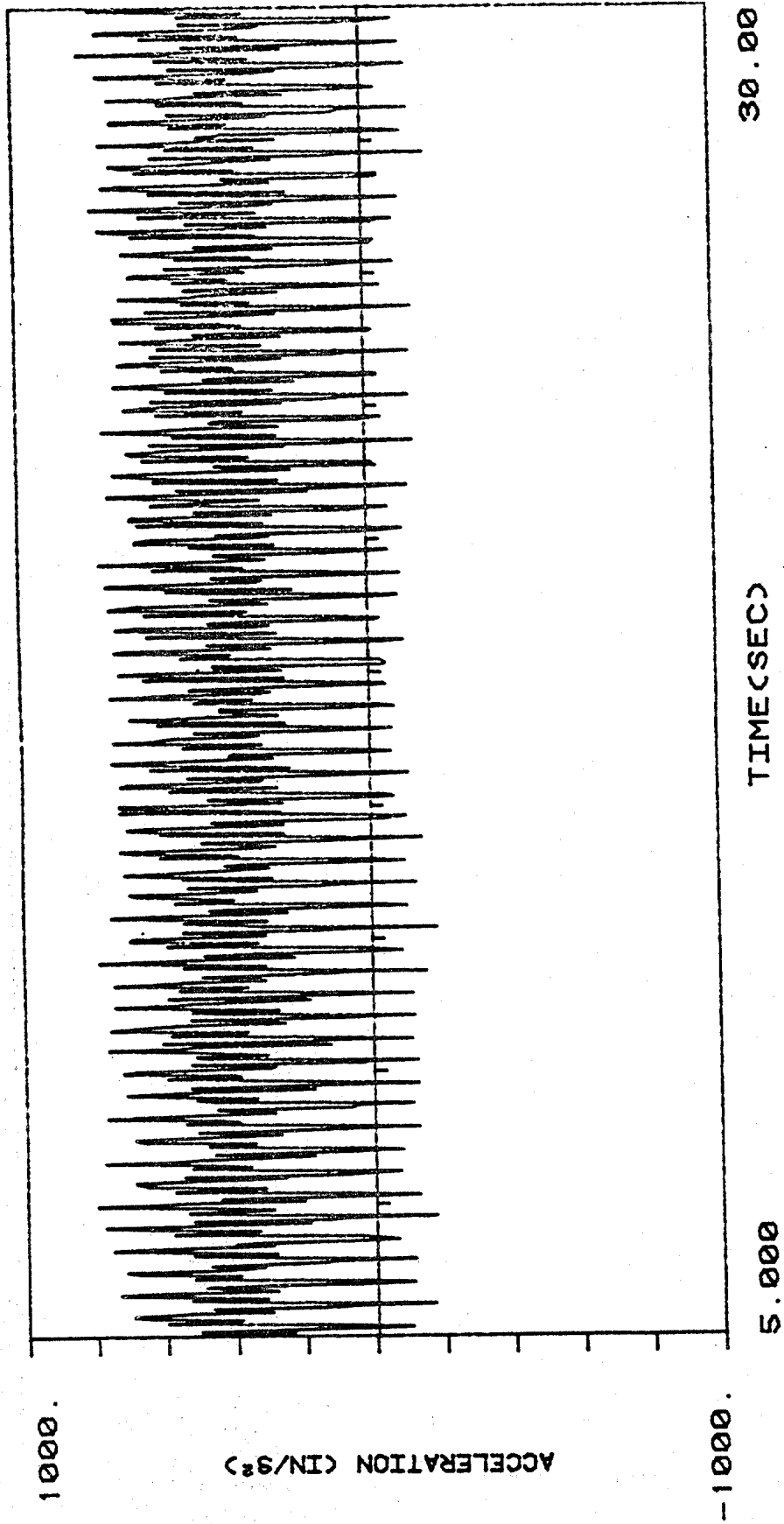


FIGURE 9. RAW VERTICAL ACCELERATION

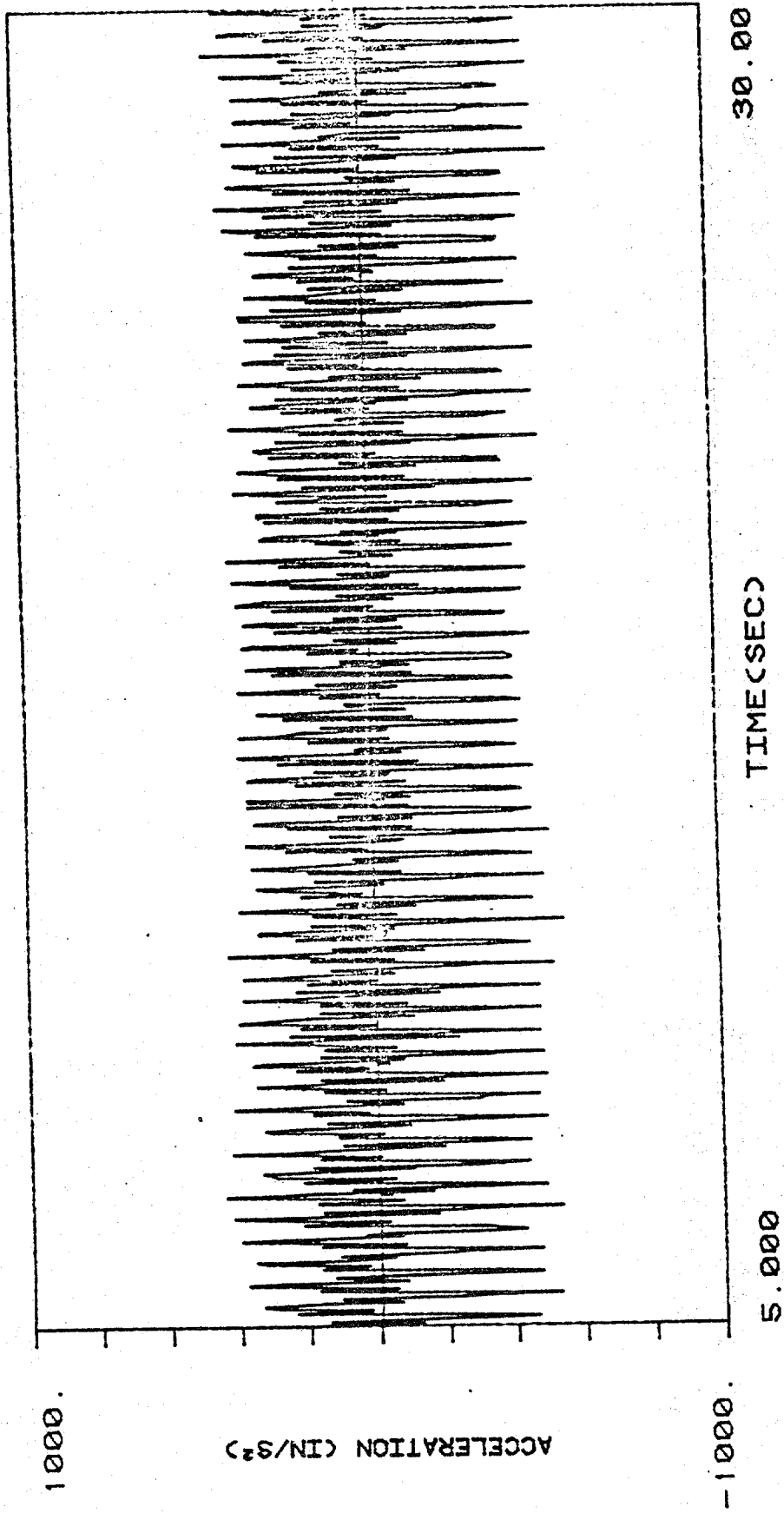


FIGURE 10. ACCELERATION AFTER INITIAL LEAST-SQUARE FIT

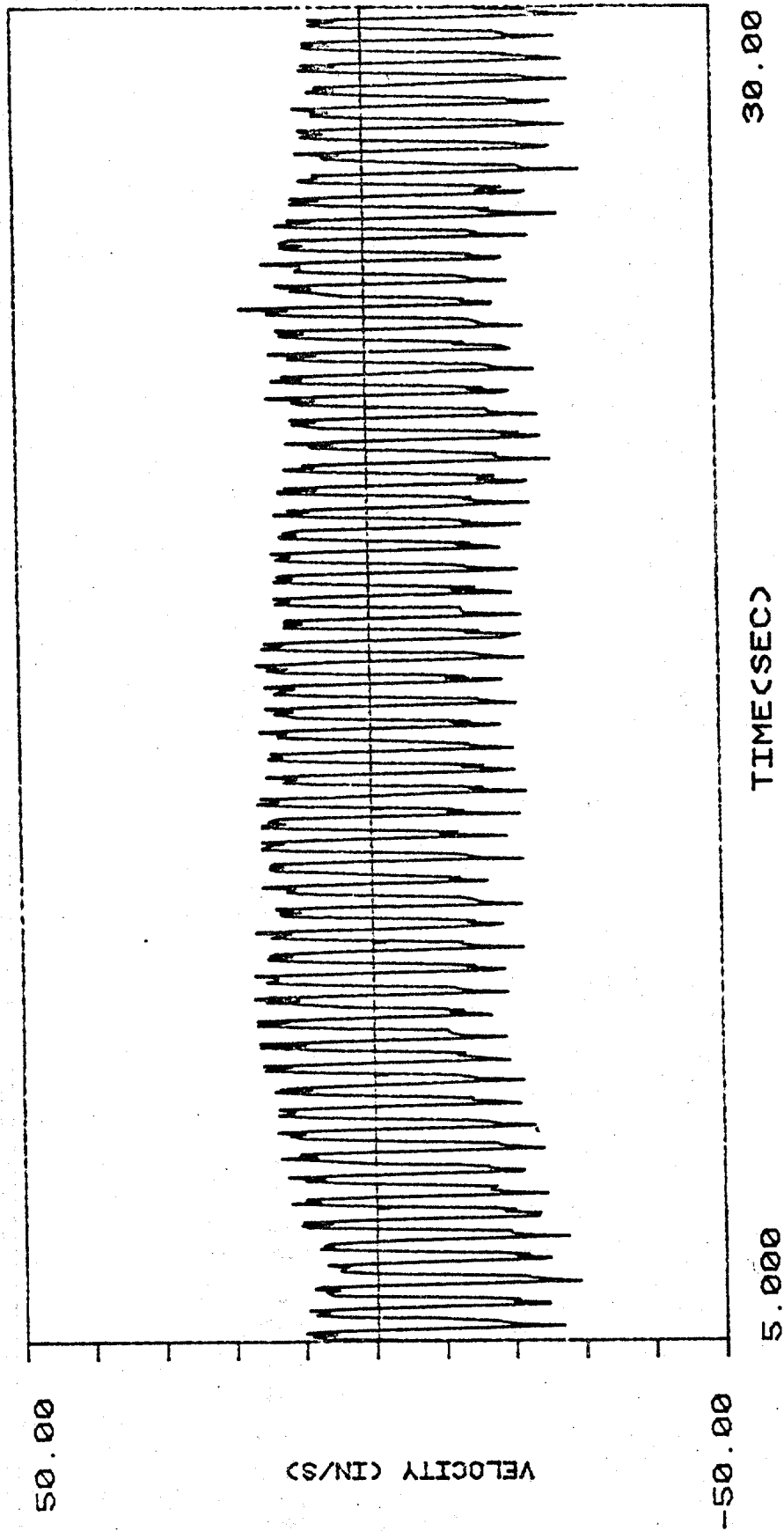


FIGURE 11. VELOCITY BEFORE HIGH-PASS FILTER

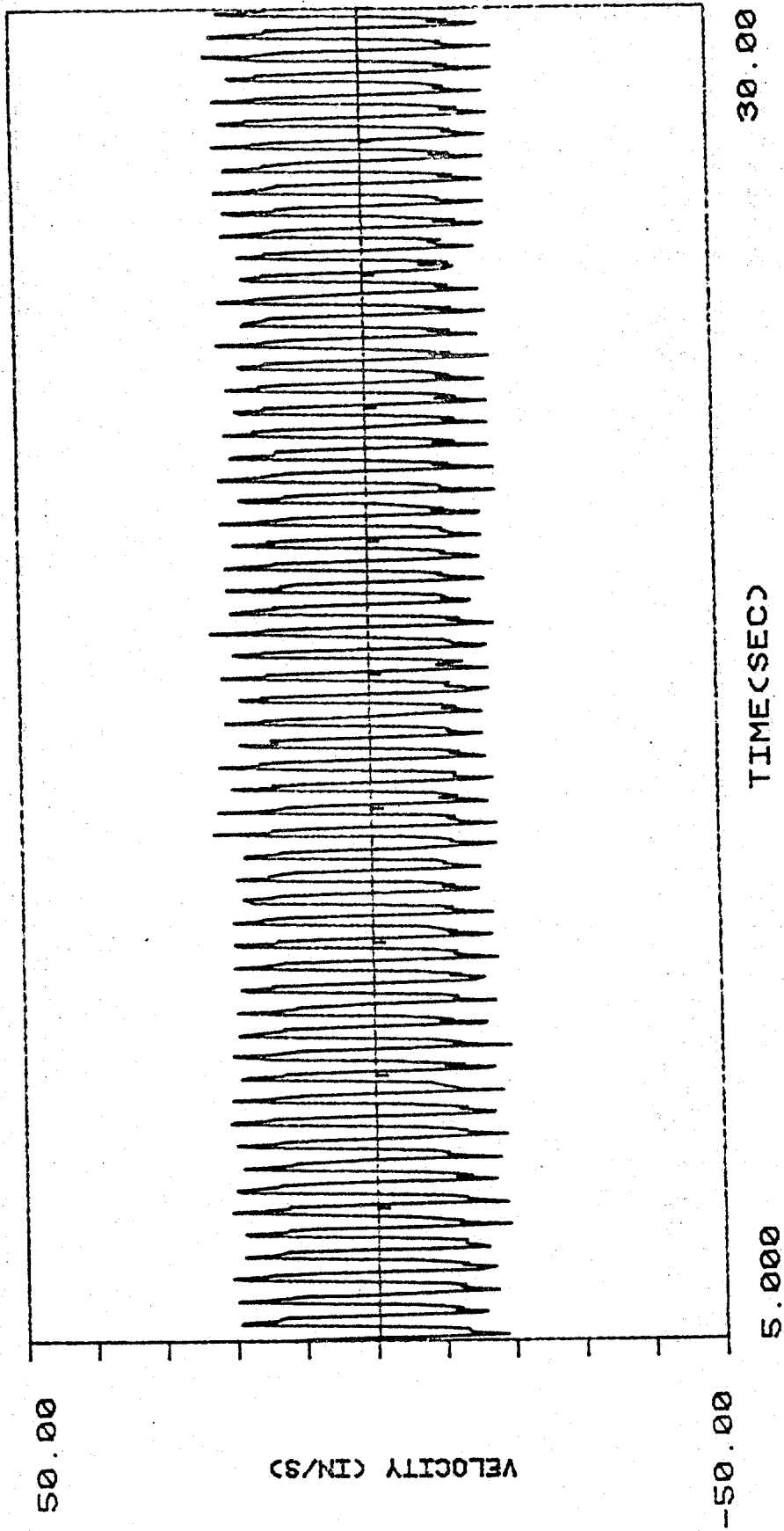


FIGURE 12. VELOCITY AFTER HIGH-PASS FILTER

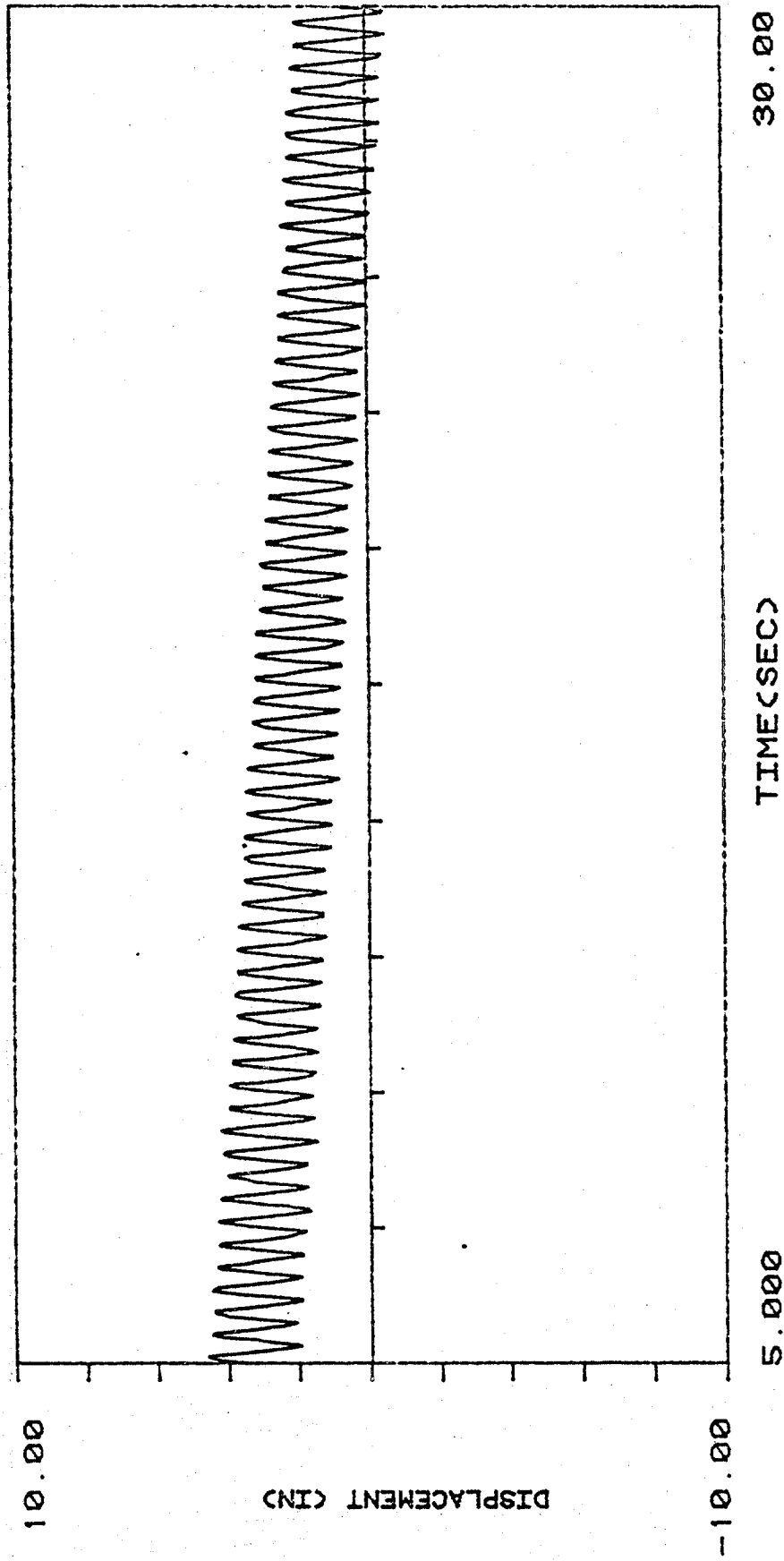


FIGURE 13. DISPLACEMENT BEFORE FINAL LEAST-SQUARE FIT

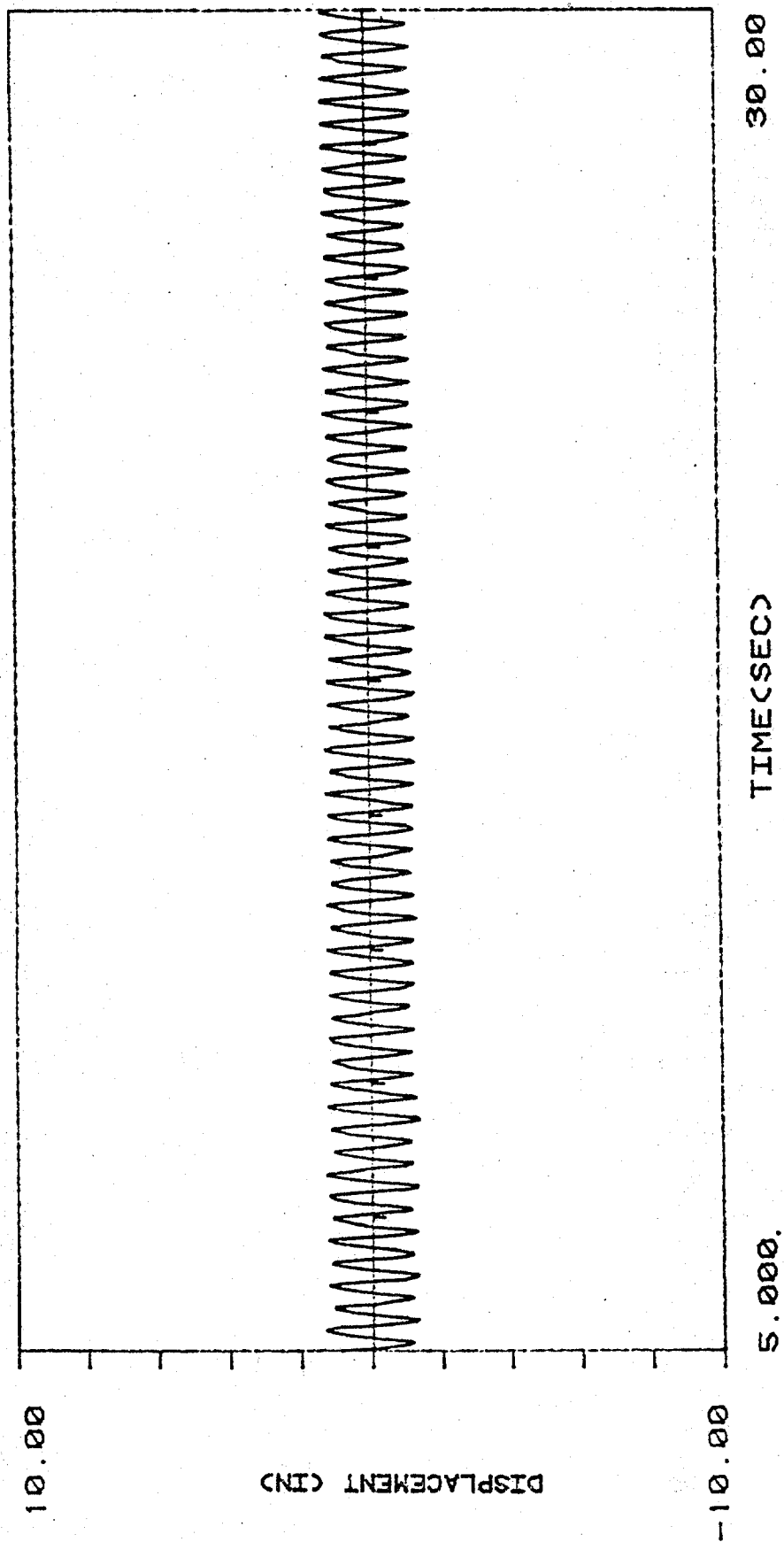


FIGURE 14. DISPLACEMENT AFTER THE FINAL LEAST-SQUARE FIT

CHAPTER V

RESULTS

5.1 2 1/2 Hour Drag Coefficient Records

Drag coefficients, for a 2 1/2 hour data cycle, were calculated for the steel tubing, bare cable, and faired cable. These records are shown in Figures 15, 17, and 19 and are plotted alongside current, vertical RMS displacement, and horizontal RMS displacement. Immediately following each of these 2 1/2 hour records, in Figures 16, 18, and 20, are the error bounds associated with each record. These error bounds are discussed in detail in Appendix B. The horizontal and vertical RMS displacements were taken from location L/6 for the steel tubing and bare cable, and from location 2L/5 for the faired cable. These RMS results represent the motion at those points and have not been adjusted or corrected for mode shape. Over the 2 1/2 hour test, many different modes are excited. Some may have nodal points near the location for which the results are plotted.

The steel tubing data gives the best illustration of the relationship between the drag coefficient and cylinder displacement. The drag coefficient and vertical RMS displacement signals show similar behavior. A sustained increase in the vertical displacement is matched by a similar increase in the drag coefficient. In addition, when the displacement exhibits large fluctuations, large fluctuations also appear in the drag coefficient. The periods of sustained increase in

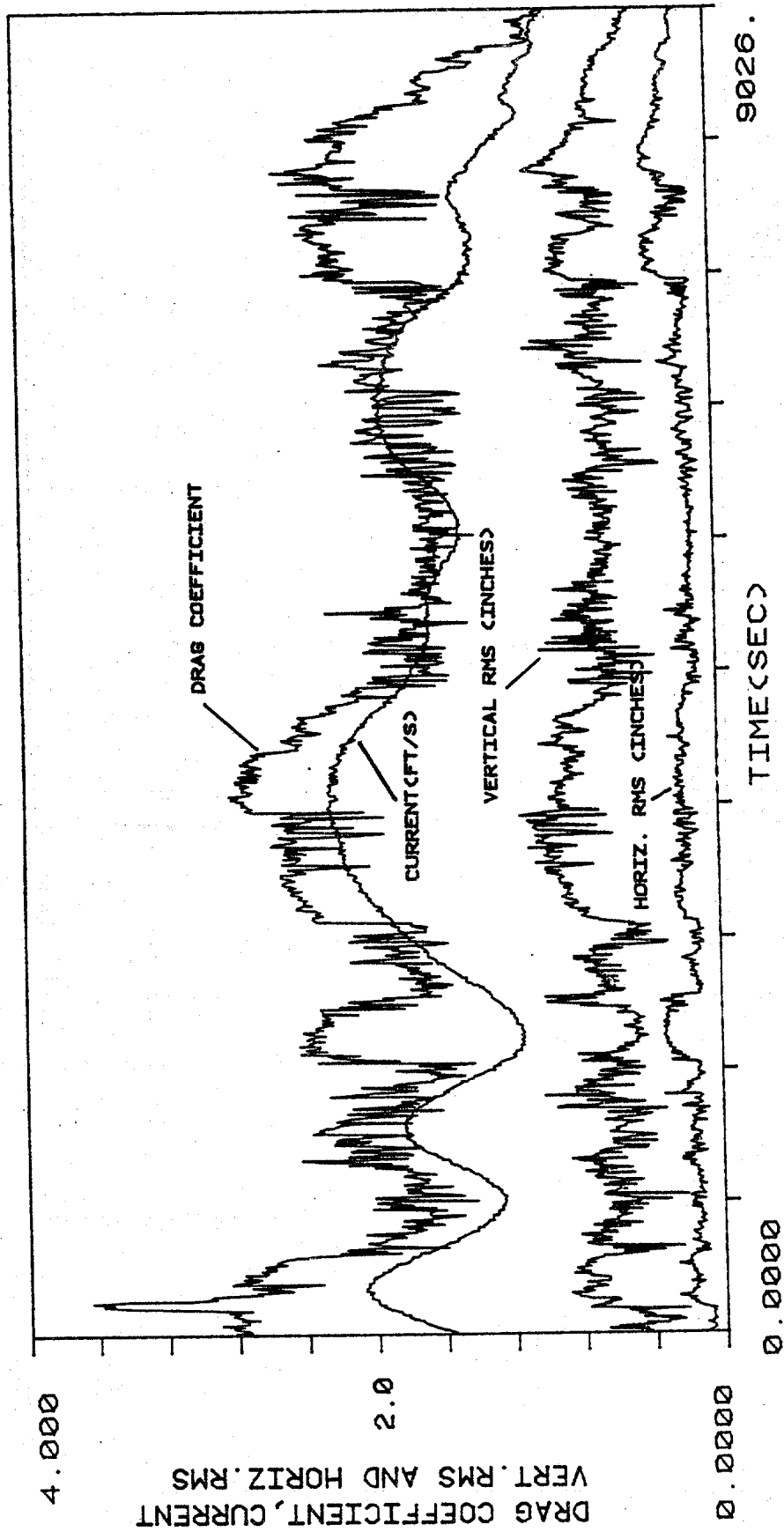


FIGURE 15. 2 1/2 HOUR STEEL TUBING RECORD.
 VERTICAL AND HORIZONTAL RMS DISPLACEMENT FROM
 ACCELEROMETER PAIR LOCATED AT L/6.

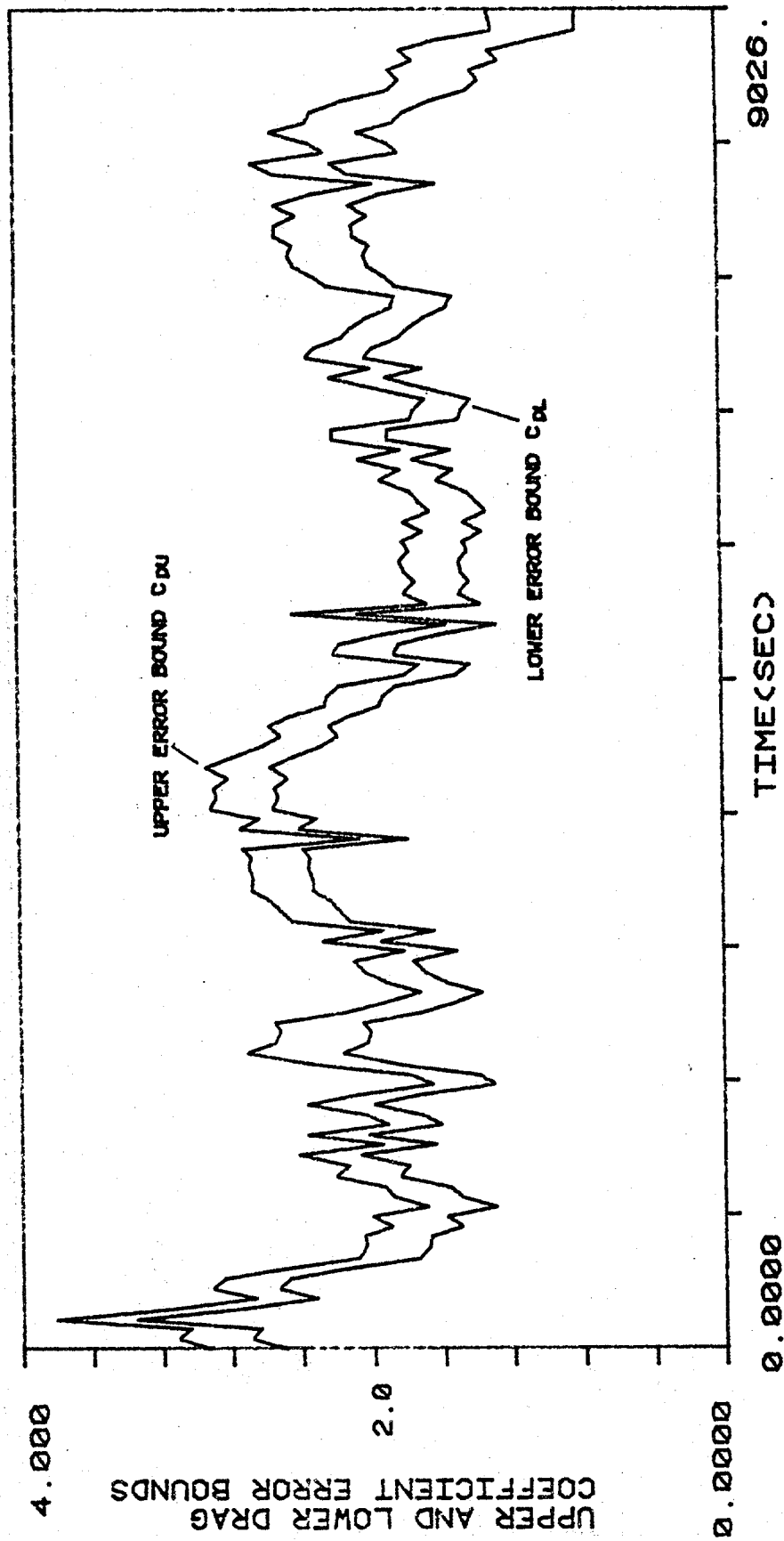


FIGURE 16. DRAG COEFFICIENT ERROR
BOUNDS FOR 2 1/2 HOUR STEEL TUBING RECORD.

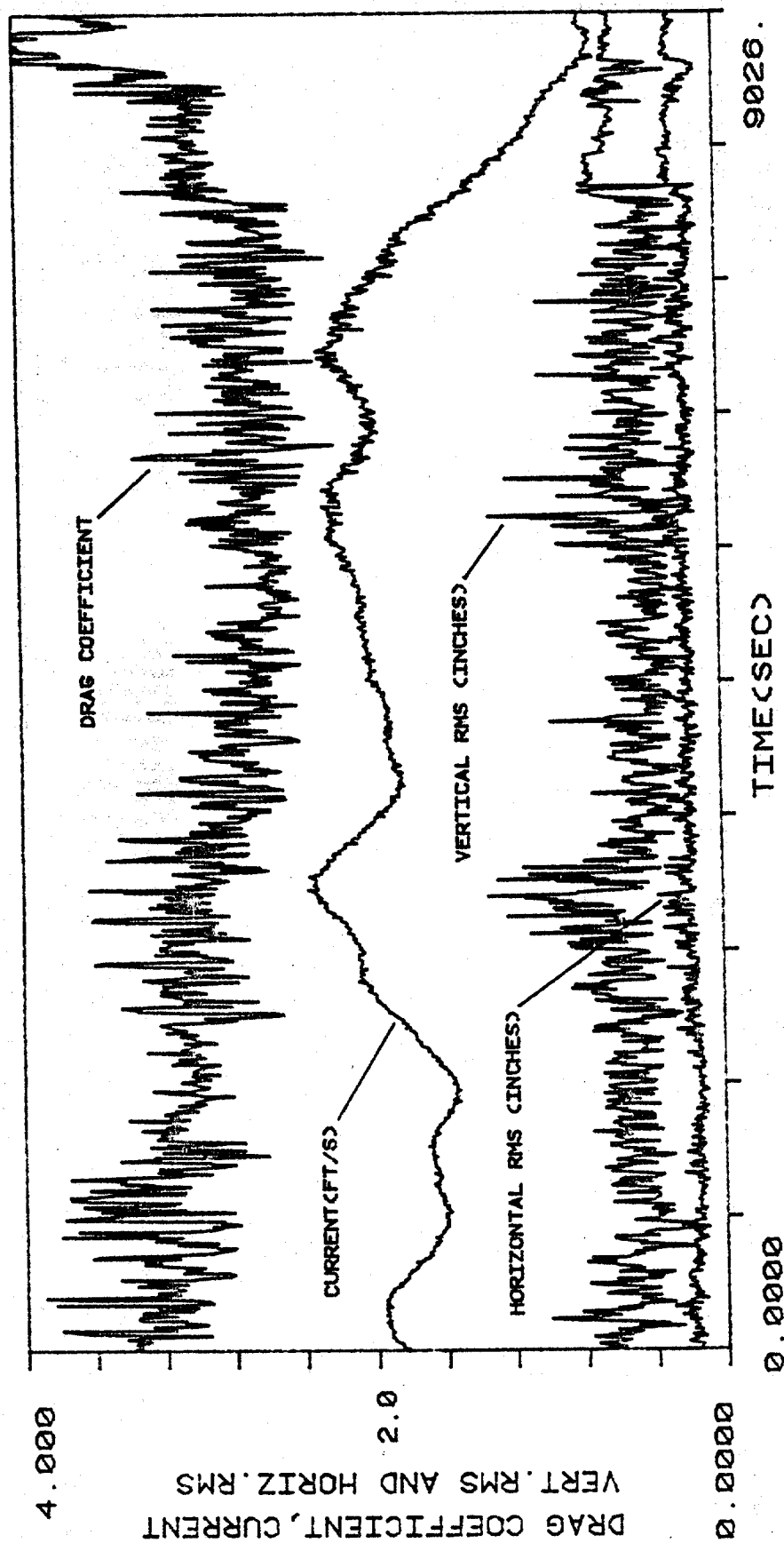


FIGURE 17. 2 1/2 HOUR BARE CABLE RECORD.
VERTICAL AND HORIZONTAL RMS DISPLACEMENT FROM
ACCELEROMETER PAIR LOCATED AT L/6.

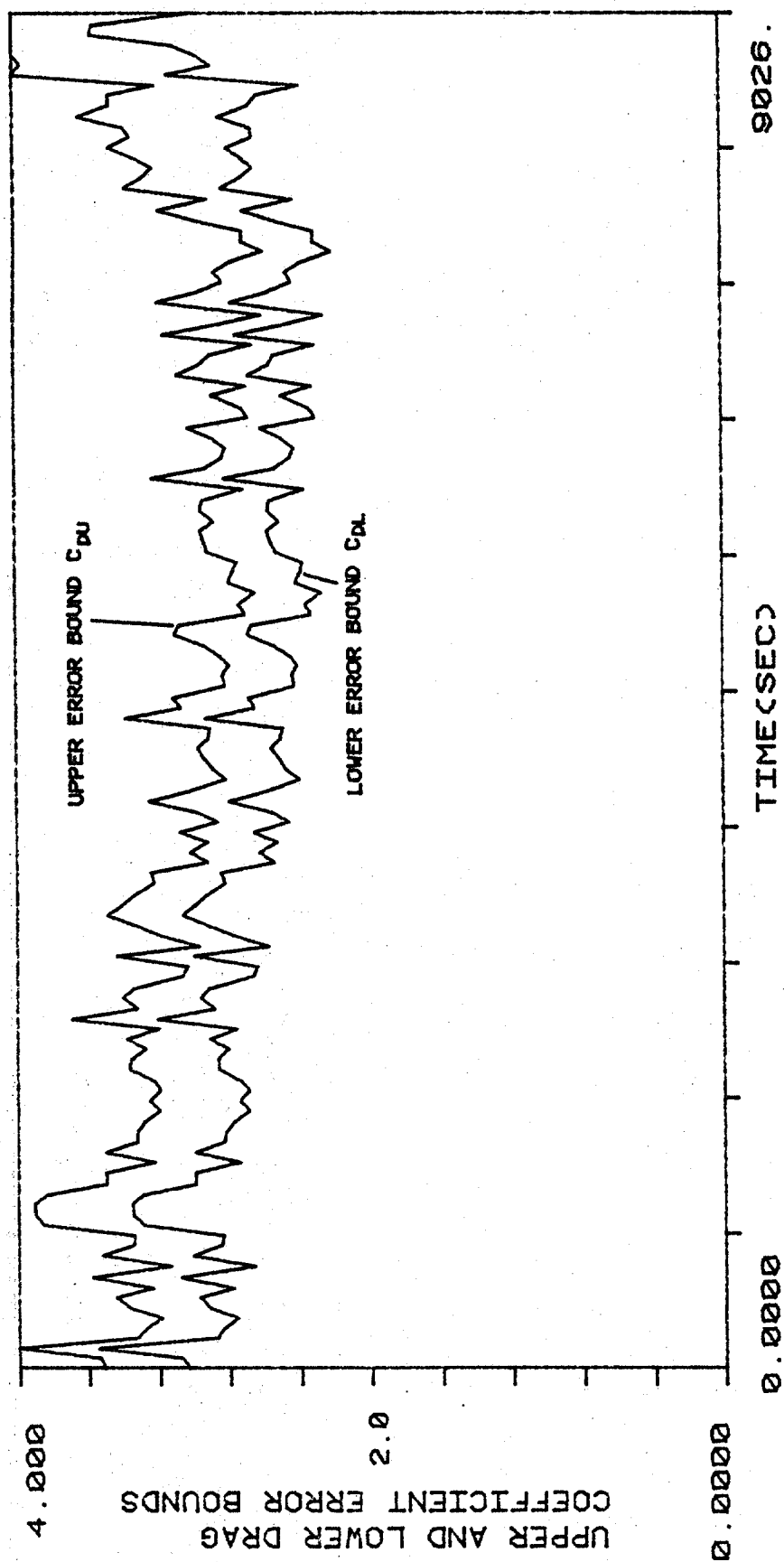


FIGURE 18. DRAG COEFFICIENT ERROR
BOUNDS FOR 2 1/2 HOUR BARE CABLE RECORD.

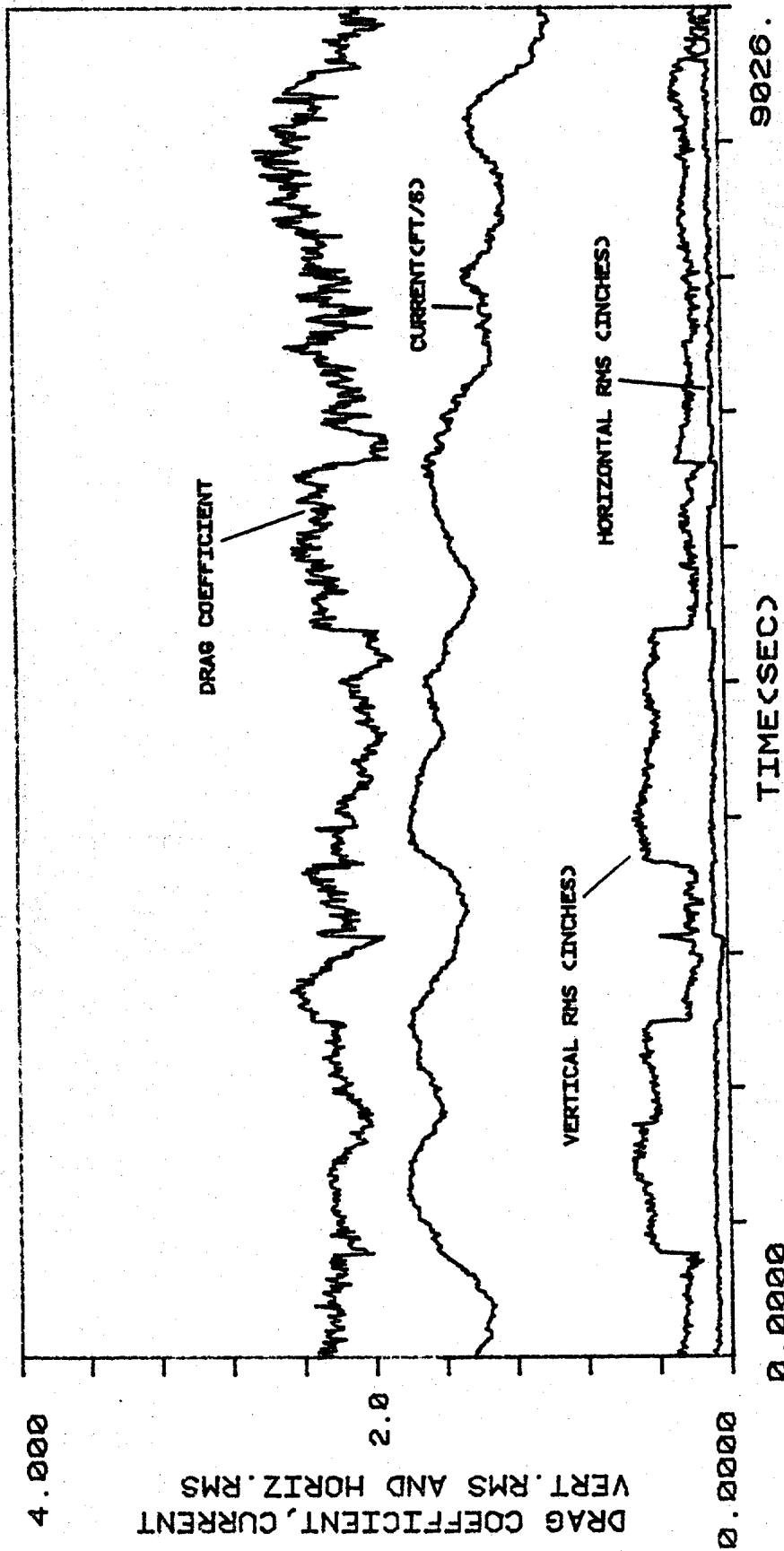


FIGURE 19. 2 1/2 HOUR FAIRED CABLE RECORD.
 VERTICAL AND HORIZONTAL RMS DISPLACEMENT FROM
 ACCELEROMETER PAIR LOCATED AT 2L/5.

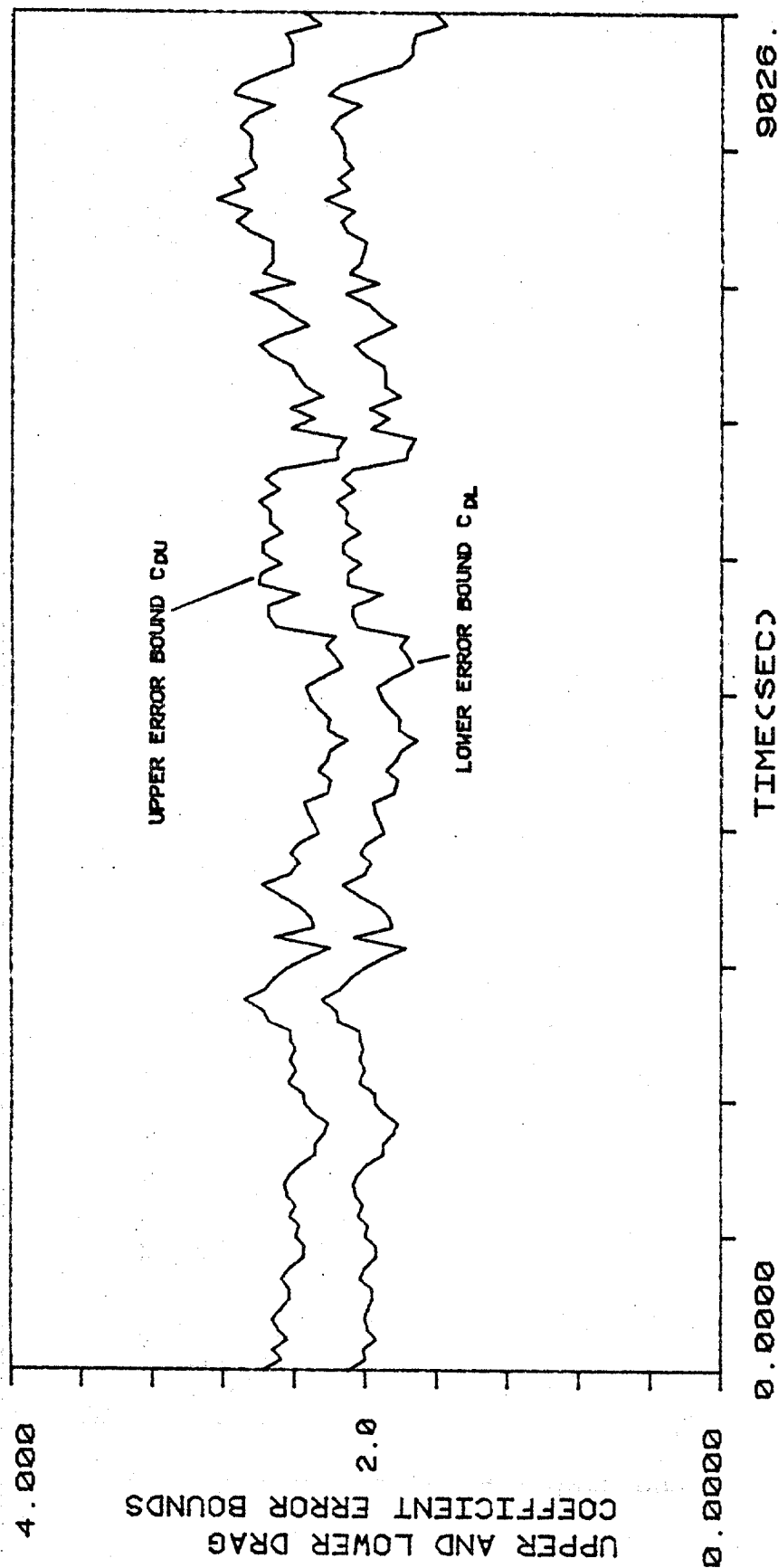


FIGURE 20. DRAG COEFFICIENT ERROR
BOUNDS FOR 2 1/2 HOUR FAIRED CABLE RECORD.

the displacement occur when the steel tubing is locked-in and responding in a single mode. During this single mode response, the fluctuations in the displacement and drag coefficient signals decrease dramatically. The regions of single mode response are much more visible in the steel tubing data than in either the bare cable or faired cable data. This is because the bending rigidity of the steel tubing causes the natural frequencies to be spaced further apart. As a result, the steel tubing is more likely to respond in a single mode and to remain in that mode for a longer period of time. The steel tube also has the lowest damping.

At one point in the steel tubing data, there is a sharp increase in the drag coefficient coinciding with a sharp increase in the horizontal displacement and no corresponding rise in the vertical displacement. In this instance, the location of the accelerometer pair was probably near a node for the vertical response.

Fewer simple observations can be made about the bare cable than the steel tubing. As was stated above, the fact that the natural frequencies of the bare cable are so close together makes it difficult for the cable to respond in one mode for very long. The drag coefficients for the bare cable are somewhat larger than those for the steel tubing. This may be due to the larger A/d ratio of the cable.

The drag coefficients for the cable with fairings are about 25% smaller than those for the bare cable. In addition, the fluctuations in the displacement and drag coefficient

signals for the faired cable are greatly reduced. The location of the accelerometer pair used in determining the vertical and horizontal displacement of the faired cable was probably near a node for one of the common vertical modes of oscillation and near and anti-node for another. This would explain the step-like appearance of the vertical RMS displacement signal.

Another interesting observation to be made from Figures 15, 17, and 19 is the difference in magnitude between the horizontal and vertical displacement of the cylinders. Previously, the consensus of opinion was that the vertical displacement was an order of magnitude greater than the horizontal displacement. However, in the results shown here, the vertical RMS displacement is only 2 to 5 times greater than the horizontal RMS displacement.

5.2 Drag Coefficients at Lock-In

The largest drag coefficients for the vibrating cylinders occur when the cylinders lock-in. During lock-in, the horizontal and vertical displacements of the cylinder are regular sinusoidal time histories. At some locations, the axis of the cylinder may exhibit a figure-eight motion. Typical examples of the vertical displacement and motion of the cylinder at lock-in are shown in Figures 21 and 22, respectively. The figure-eight motion of the cylinder illustrates the fact that the horizontal response frequency of the cylinder is twice the vertical response frequency when the cylinder is locked-in. For every vertical cycle, the cylinder

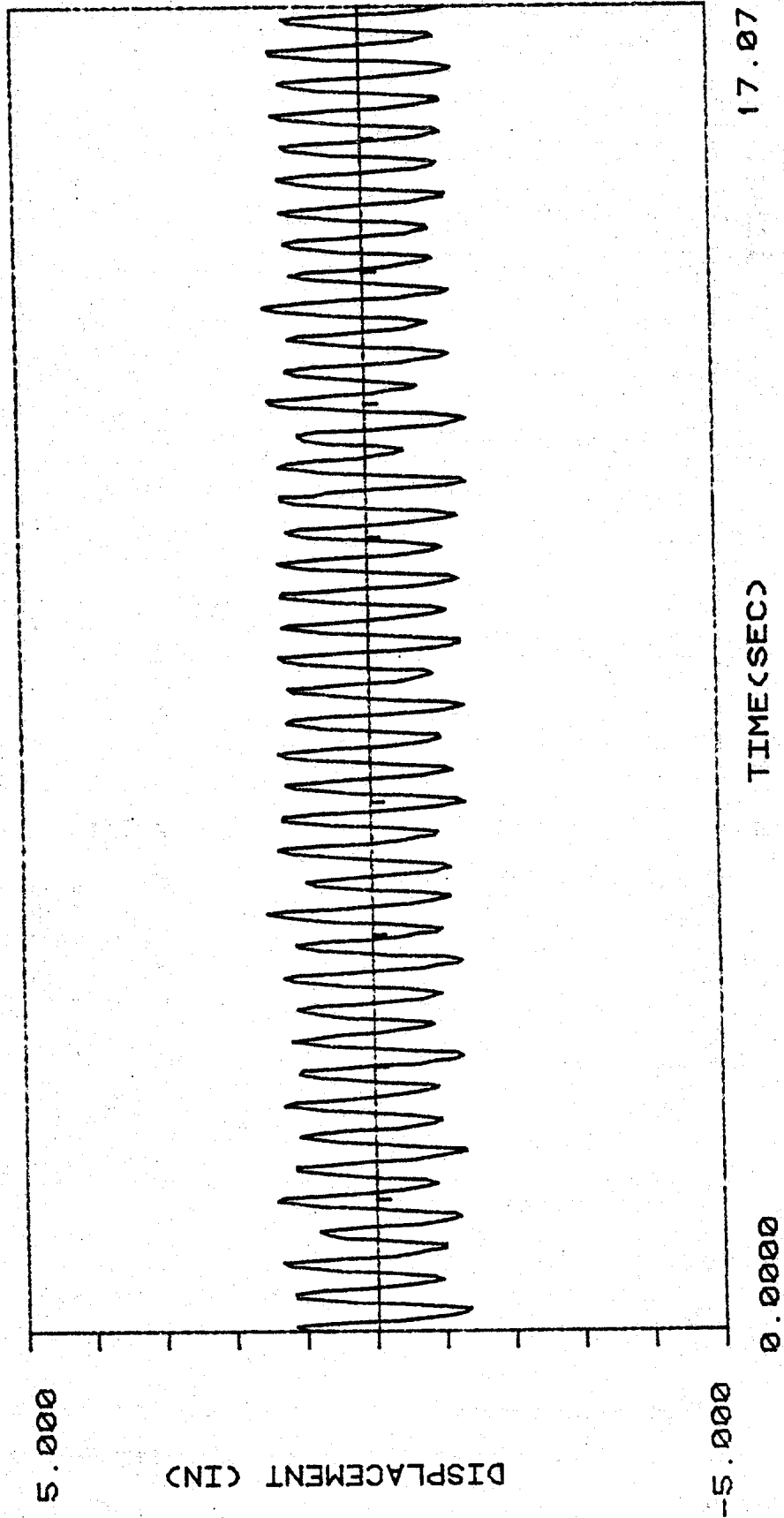


FIGURE 21. VERTICAL DISPLACEMENT TIME HISTORY OF THE
STEEL TUBING AT LOCK-IN. POSITION L/6.

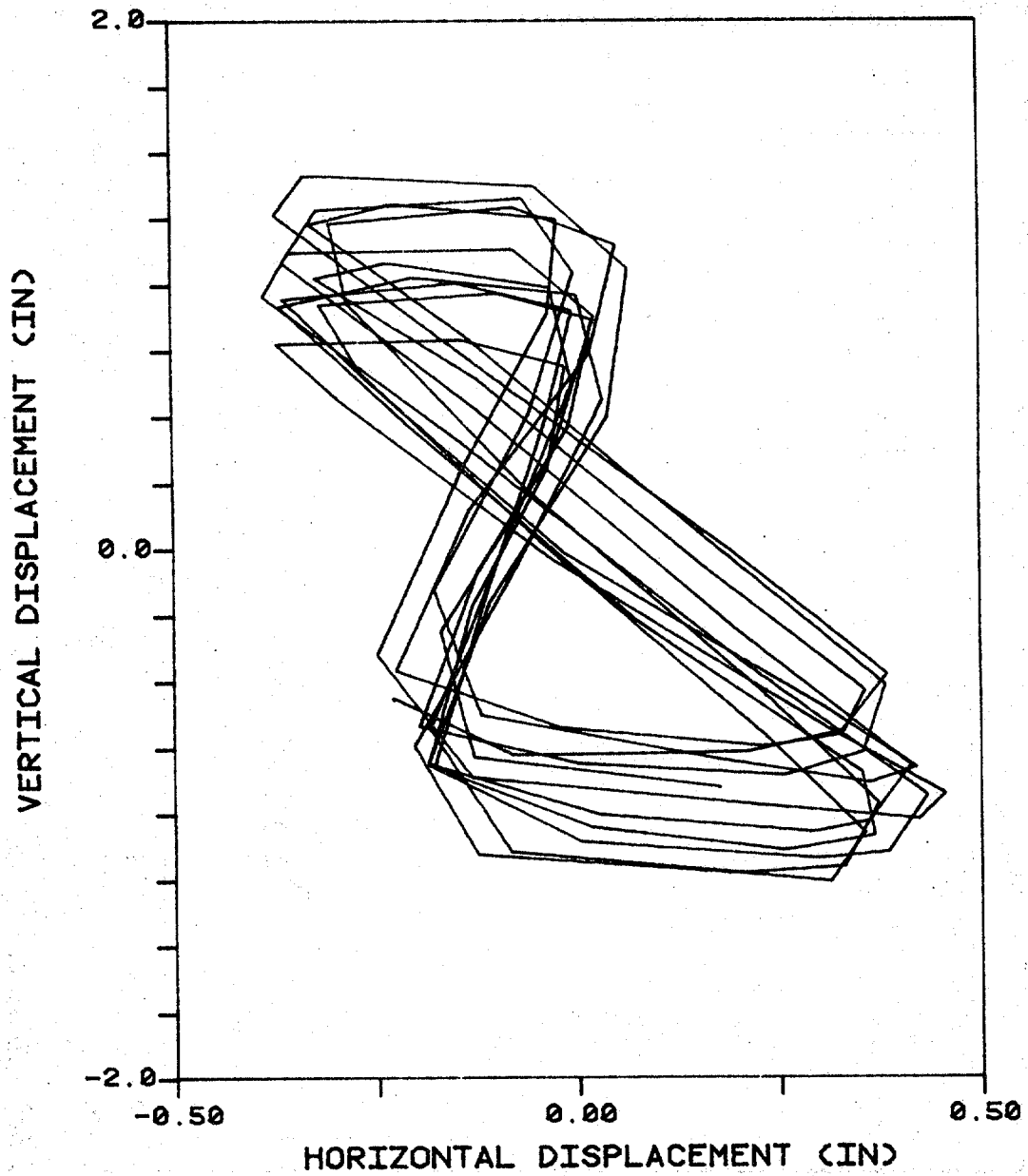


FIGURE 22. LOCK-IN MOTION OF
THE STEEL TUBING AT POSITION L/6.

must go through two horizontal cycles to complete a figure-eight. The horizontal and vertical motions represent the response of different modes. In one example, the vertical motion of the pipe was third mode, while the horizontal motion was fifth mode. This is because for the pipe the fifth mode natural frequency is two times the third mode.

FFTs of the tubing and cable at lock-in are shown in Figures 23 and 24, respectively. These figures show that at lock-in the motion of the cylinders is dominated by one mode.

Plots of the drag coefficient along with current, vertical RMS displacement, and horizontal RMS displacement for the steel tubing and bare cable at lock-in are shown in Figures 25 through 28. The location of the accelerometer pair used to determine the RMS displacements was at $L/6$.

In Figure 25, the steel tubing is oscillating vertically in the third mode and horizontally in the fifth mode. Since the accelerometer pair was located at $L/6$, the vertical RMS displacement will be that of an anti-node and the horizontal RMS displacement will be for a position near a node. For this example, the drag coefficient has a fairly constant value of about 2.5 except at several points where, for some unknown reason, dropouts occur. Similar dropouts also occur at the same time in the vertical and horizontal RMS displacement of the tubing which supports the theory that the drag force on an oscillating cylinder is highly dependent on its displacement. In Figure 26, the steel tubing is again responding

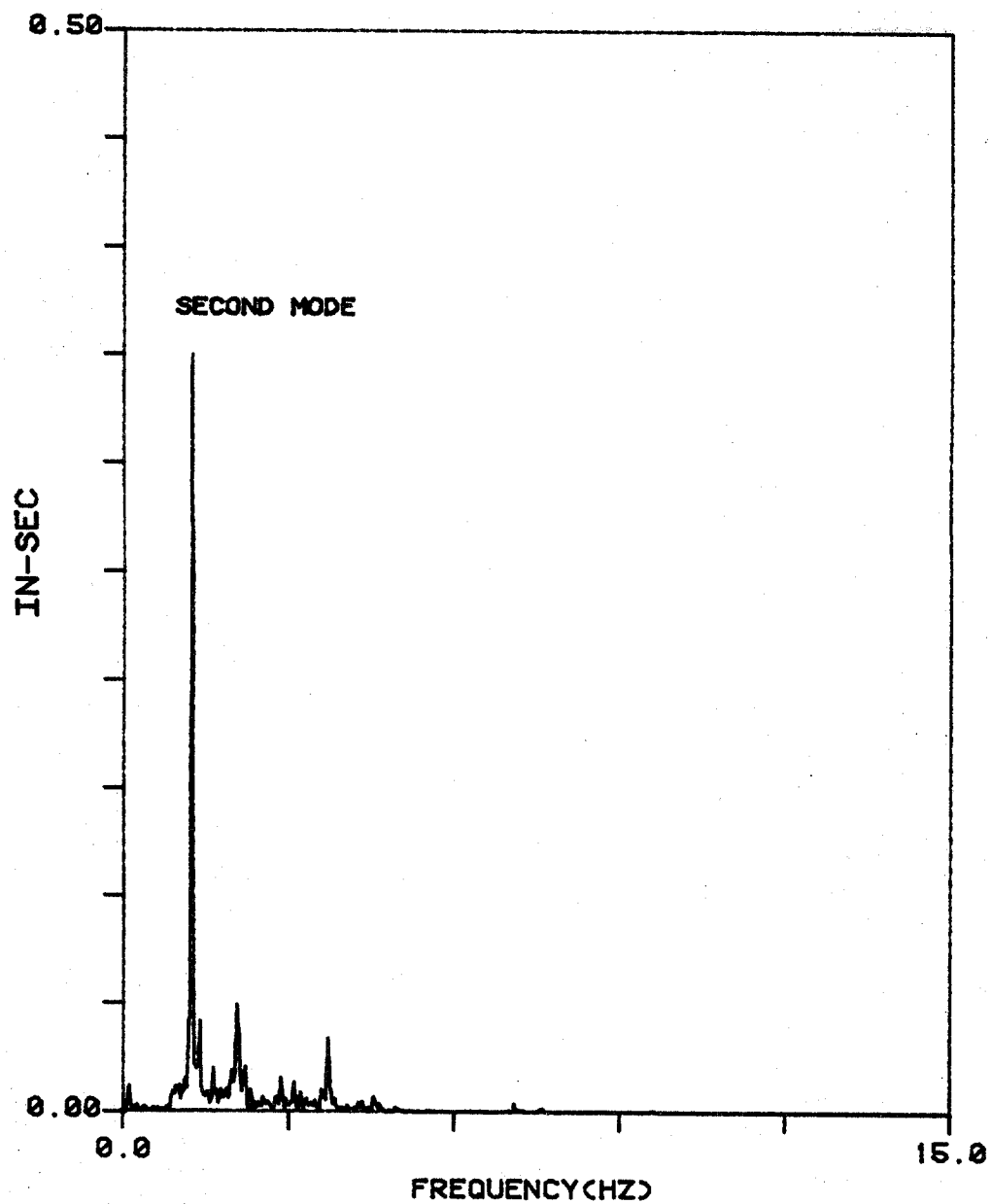


FIGURE 23. FFT OF THE STEEL
TUBING AT LOCK-IN. VERTICAL
DISPLACEMENT AT POSITION L/6.

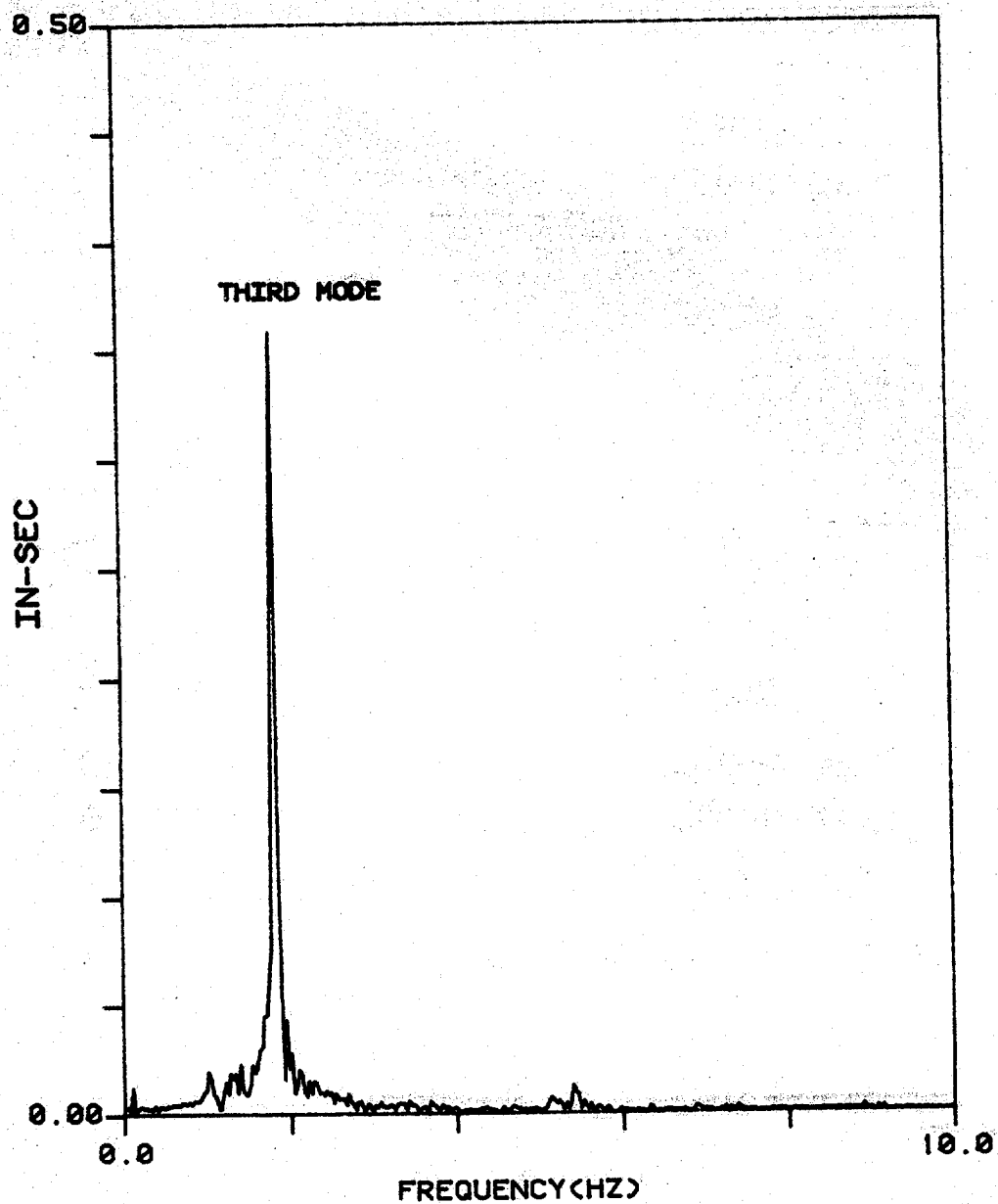


FIGURE 24. FFT OF THE BARE
CABLE AT LOCK-IN. VERTICAL
DISPLACEMENT AT POSITION $L/6$.

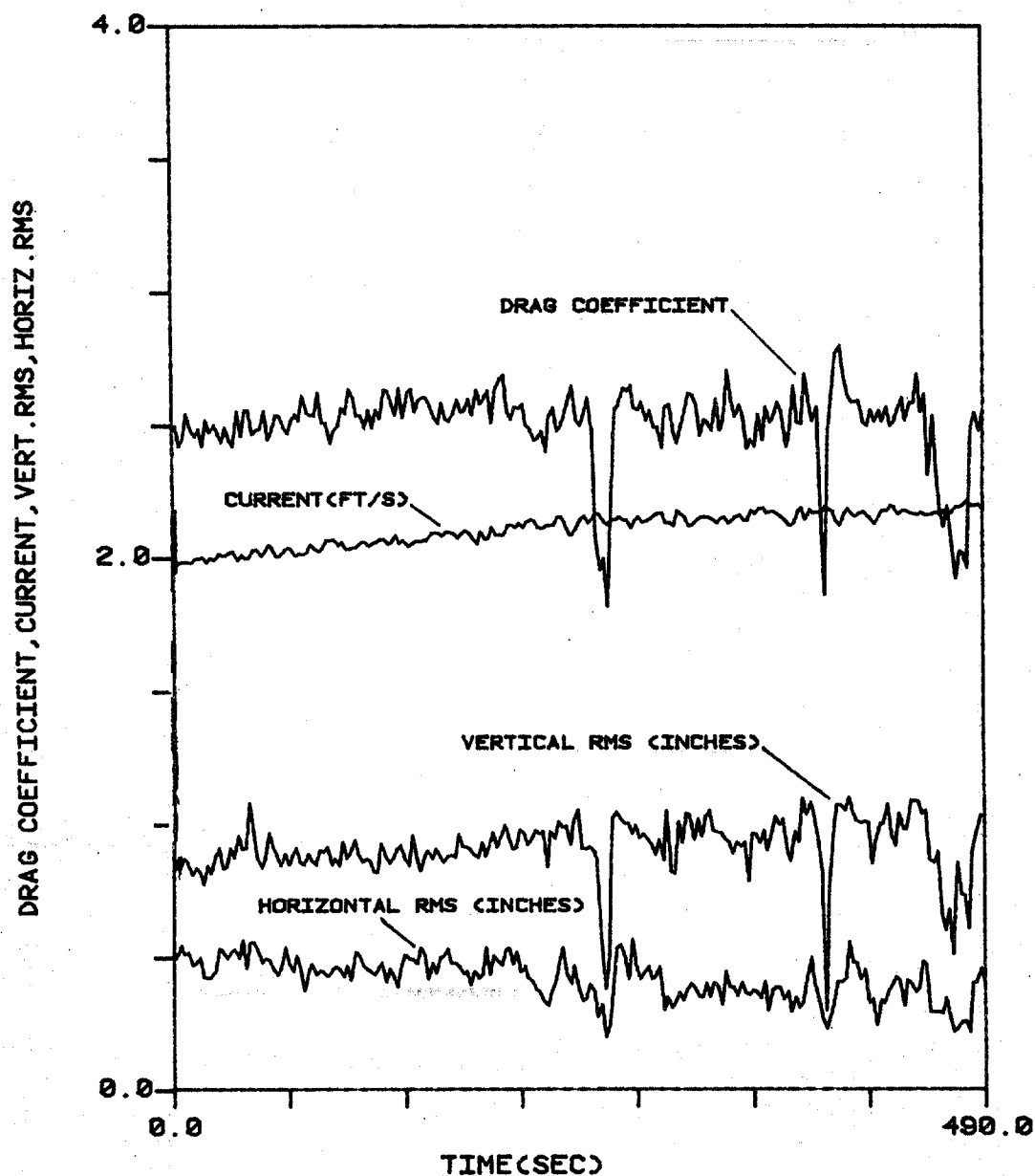


FIGURE 25. STEEL TUBING DURING
THIRD MODE VERTICAL AND FIFTH MODE
HORIZONTAL RESPONSE. ACCELEROMETER
PAIR LOCATED AT L/6.

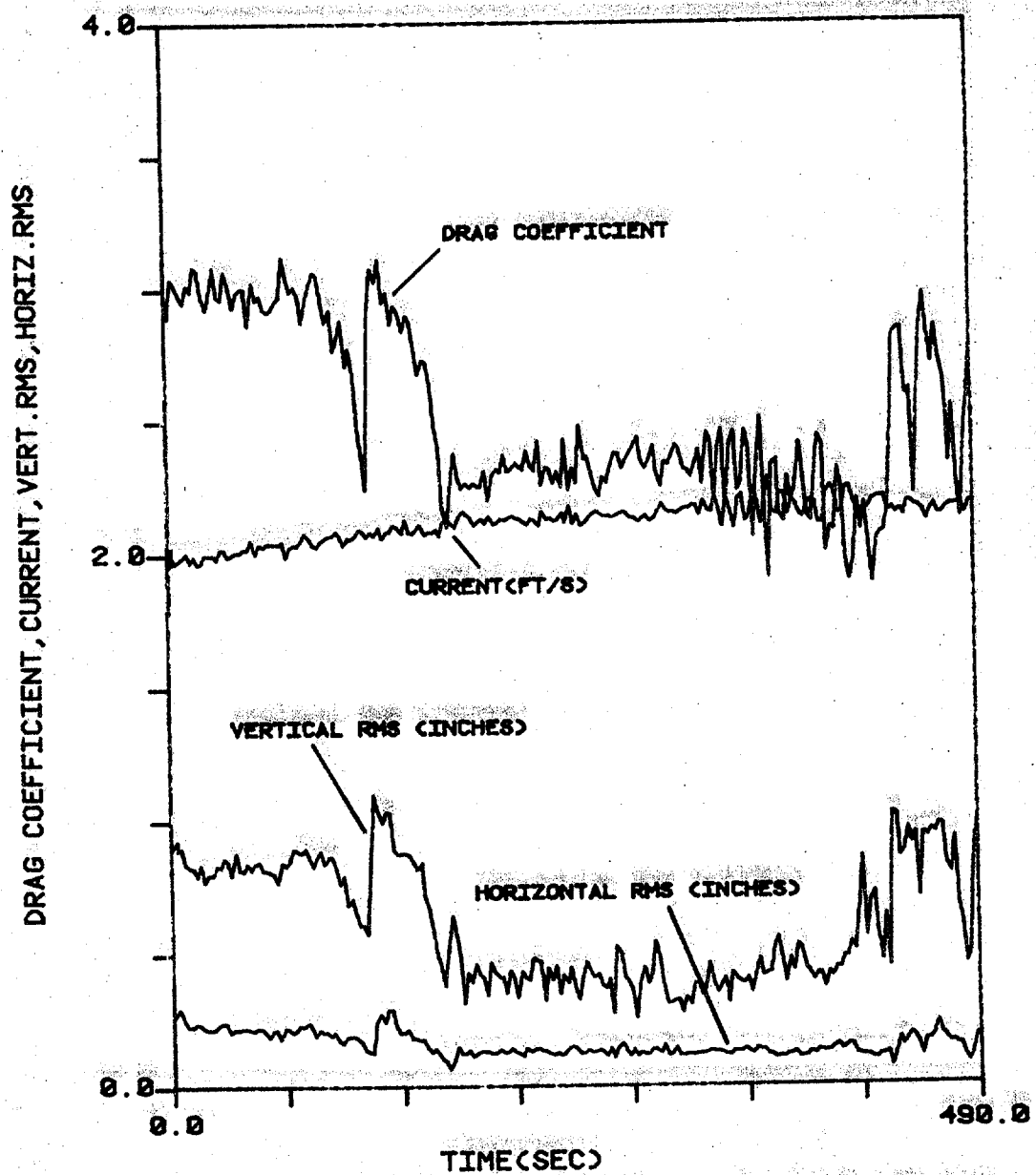


FIGURE 26. STEEL TUBING. THIRD MODE VERTICAL AND FIFTH MODE HORIZONTAL RESPONSE DECAYING TO RANDOM RESPONSE. ACCELEROMETER PAIR AT L/6.

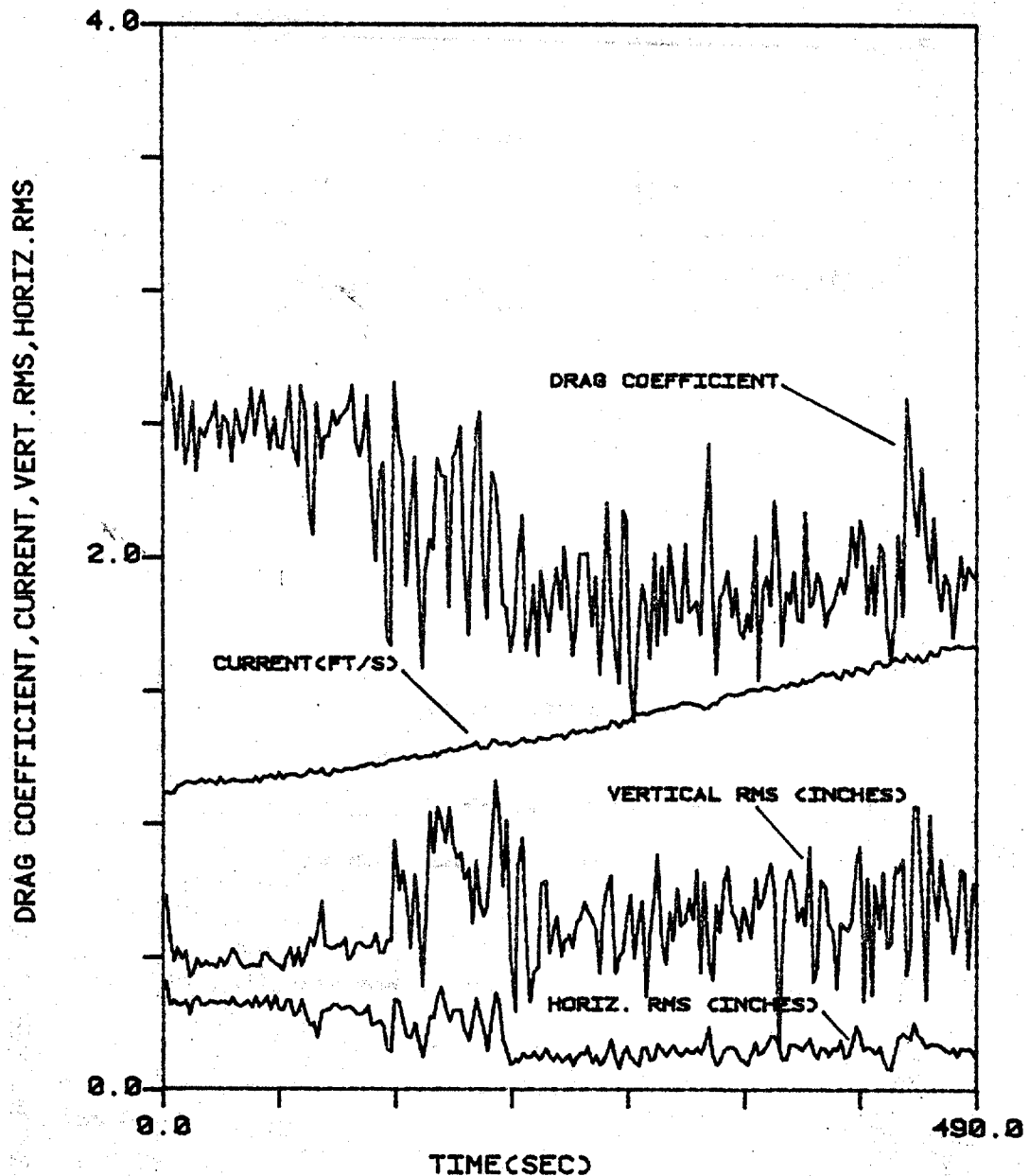


FIGURE 27. STEEL TUBING. SECOND MODE VERTICAL AND THIRD MODE HORIZONTAL RESPONSE DECAYING TO RANDOM RESPONSE. ACCELEROMETER PAIR AT L/6.

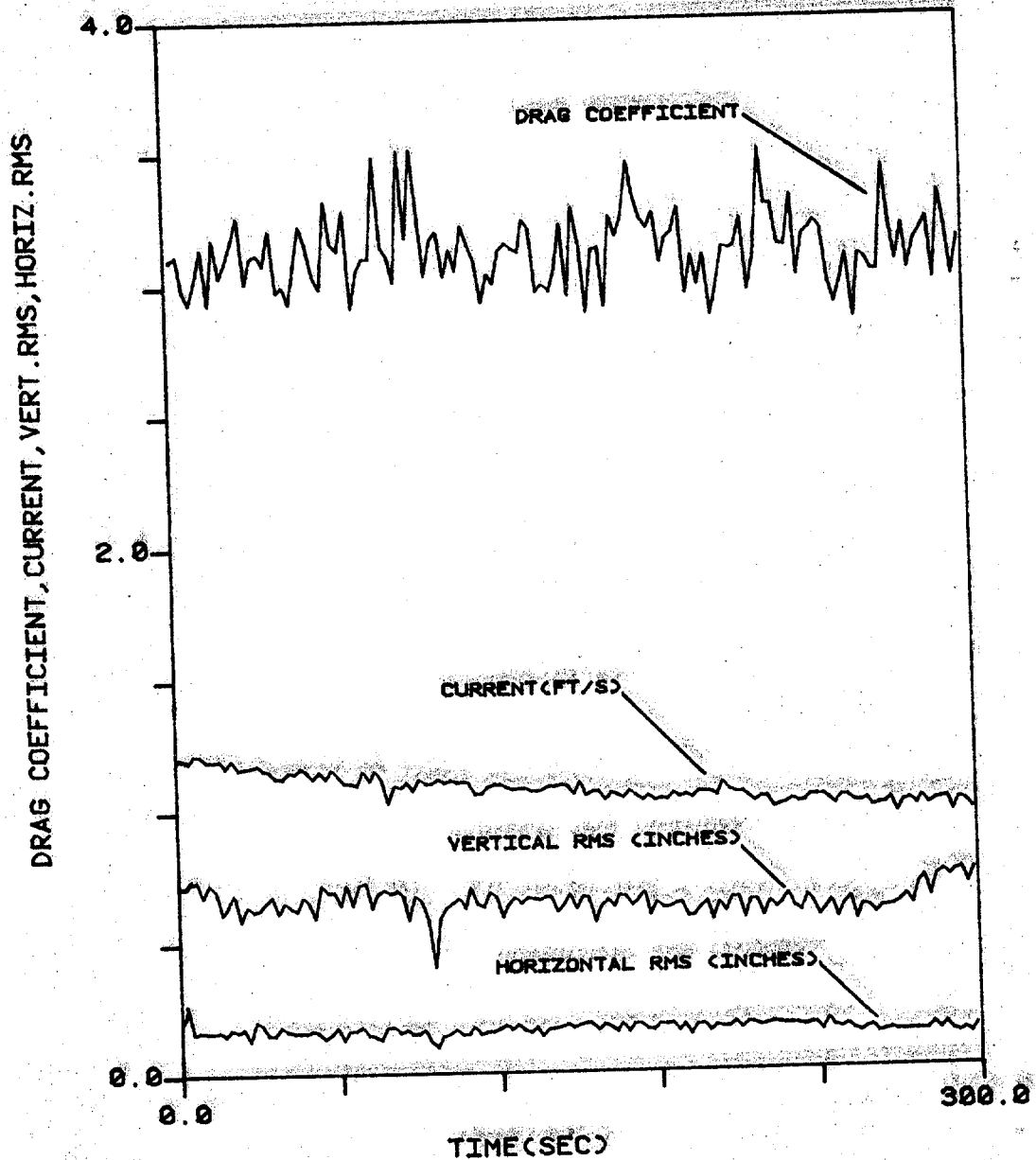


FIGURE 28. BARE CABLE DURING
THIRD MODE VERTICAL AND FIFTH MODE
HORIZONTAL RESPONSE. ACCELEROMETER
PAIR LOCATED AT L/6.

vertically in the third mode and horizontally in the fifth mode. However, this locked-in behavior decays to a non locked-in state about 2 1/2 minutes into the record. During this 2 1/2 minutes of lock-in behavior, the drag coefficient has a value of 3.0. In Figure 27, the steel tubing is initially responding vertically in the second mode and horizontally in the third mode. However, as in the previous figure, the locked-in behavior decays to a non locked-in state after about 2 minutes. For this case, the accelerometer pair is located at an anti-node for the horizontal mode and at an intermediate position for the vertical mode. The drag coefficient has an average value of about 2.5 while the steel tubing is locked-in and this drops to around 1.9 with large fluctuations when the tubing begins to respond randomly.

Figure 28 shows an example of the bare cable when it was responding vertically in the third mode and horizontally in the fifth mode. For this case, the average drag coefficient can be seen to be about 3.15. The drag coefficients calculated from the bare cable data are higher than those from the steel tubing. As was stated before, one possible explanation for this is the larger A/d ratio of the bare cable.

5.3 Non Lock-In Drag Coefficients

When the vortex shedding process and the cylinder motion are not locked-in, the cylinder will respond in some random manner. Typical examples of the vertical displacement and real time motion of the cylinder during this random response are given in Figures 29 and 30, respectively. These figures

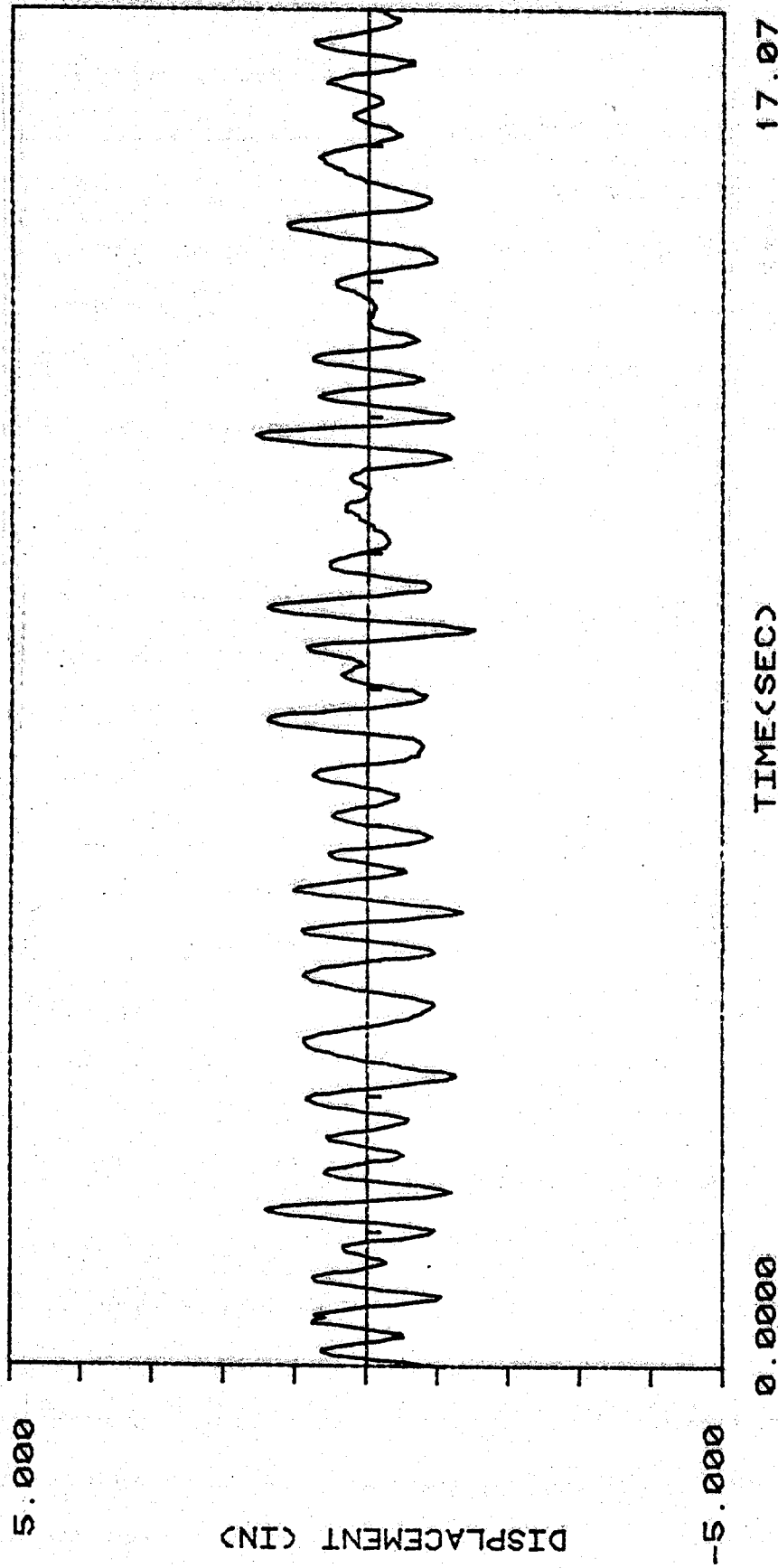


FIGURE 29. NON LOCK-IN VERTICAL DISPLACEMENT TIME HISTORY OF THE STEEL TUBING. POSITION L/6.

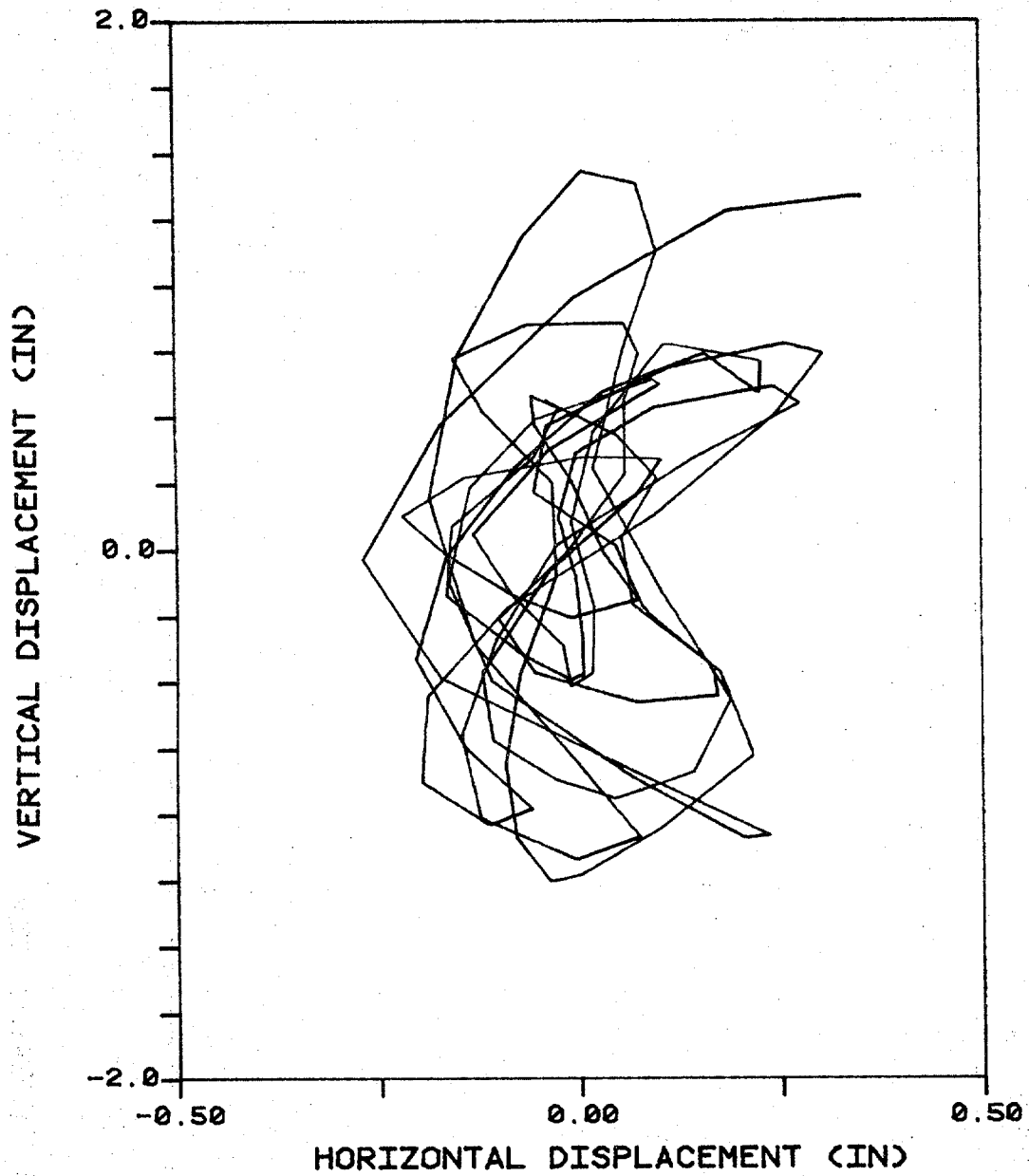


FIGURE 30. NON LOCK-IN MOTION OF
THE STEEL TUBING AT POSITION L/6.

show that, unlike the locked-in case, the displacement of the cylinder is no longer uniform and the motion of the cylinder is no longer a distinct figure-eight.

FFTs of the steel tubing and bare cable during non lock-in response are given in Figures 31 and 32, respectively. These figures show how the energy in the cylinder is spread over a wider frequency range when the cylinder is not locked-in.

Drag coefficient examples for the steel tubing and bare cable during this non lock-in behavior are shown in Figures 33 and 34, respectively. These figures show that the drag coefficients during non lock-in response are lower than their locked-in counterparts. In addition, the fluctuations in the drag coefficient, vertical RMS displacement, and horizontal RMS displacement signals are larger in the non locked-in examples.

5.4 Predicted Drag Coefficients

Drag coefficient predictions were performed for a locked-in steel tubing test and a locked-in bare cable test using Equation 2.12. The results of these predictions are shown in Figures 35 and 36. The amplitude (A) used in Equation 2.12 was the vertical RMS displacement of the cylinders at position $L/6$. In the predicted drag coefficient examples, both the steel tubing and the bare cable were responding vertically in the third mode. Therefore, position $L/6$ is an antinode and represents the model amplitude of the cylinder. In the steel tubing case, the predicted

drag coefficient underestimated the measured drag coefficient by about 14% except at the dropouts where the measured and predicted values were almost the same. In addition, the form of the predicted and measured drag coefficient signals were quite similar. On the other hand, the shapes of the predicted and measured drag coefficient signals for the bare cable were quite different and the predicted values underestimated the measured values by 28%.

Appendix D presents an example of drag coefficient data for a cable with lumped masses.

CHAPTER VICONCLUSIONS

The drag coefficient for a long flexible cylinder excited by vortex shedding is much larger than that for stationary cylinders. Maximum drag coefficients of about 3.3 for the bare cable and 3.0 for the pipe are seen in the data. The stationary drag coefficient value for the Reynolds number encountered is about 1.175.

For the steel tubing, the largest drag coefficients occurred when the cylinder was locked-in. During lock-in, the RMS displacement of the steel tubing was also maximum and the fluctuations in both the drag coefficient and RMS displacement signals reduced dramatically. At non-lock-in the mean drag coefficient was lower, but was accompanied by large fluctuations in drag coefficient and response amplitude.

The bare cable's lock-in regions are less distinct than the steel tubing's. The closer spacing of natural frequencies in the bare cable makes it more difficult for it to respond in a single mode for very long. The bare cable drag coefficient time history shows less variation over the 2 1/2 hour record than the steel tubing making it more difficult to detect regions of locked-in response. On the other hand, the high frequency fluctuations in the drag coefficient and RMS displacement signals are greater in the bare cable data than in the steel tubing data.

The application of the long stranded plastic fairings to the bare cable reduced the drag coefficient by about 25%. In addition, these fairings reduced the fluctuations in both the drag coefficient and RMS displacement signals.

Finally, the predicted drag coefficients, found by using the method described by Griffin [5], underestimated the measured drag coefficient by 14% in the steel tubing test and 28% in the bare cable test.

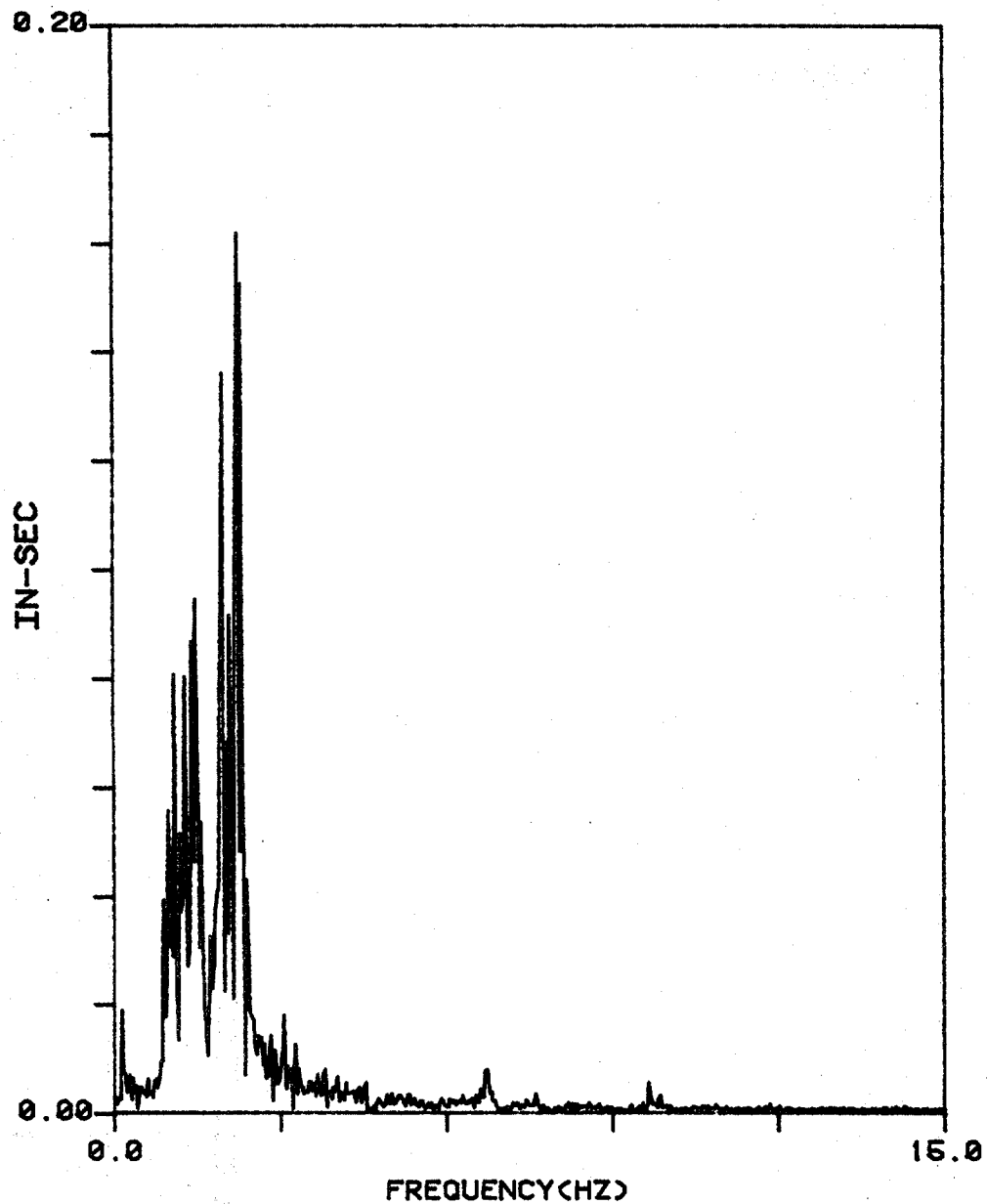


FIGURE 31. FFT OF THE STEEL TUBING
DURING NON LOCK-IN RESPONSE
VERTICAL DISPLACEMENT AT POSITION L/6.

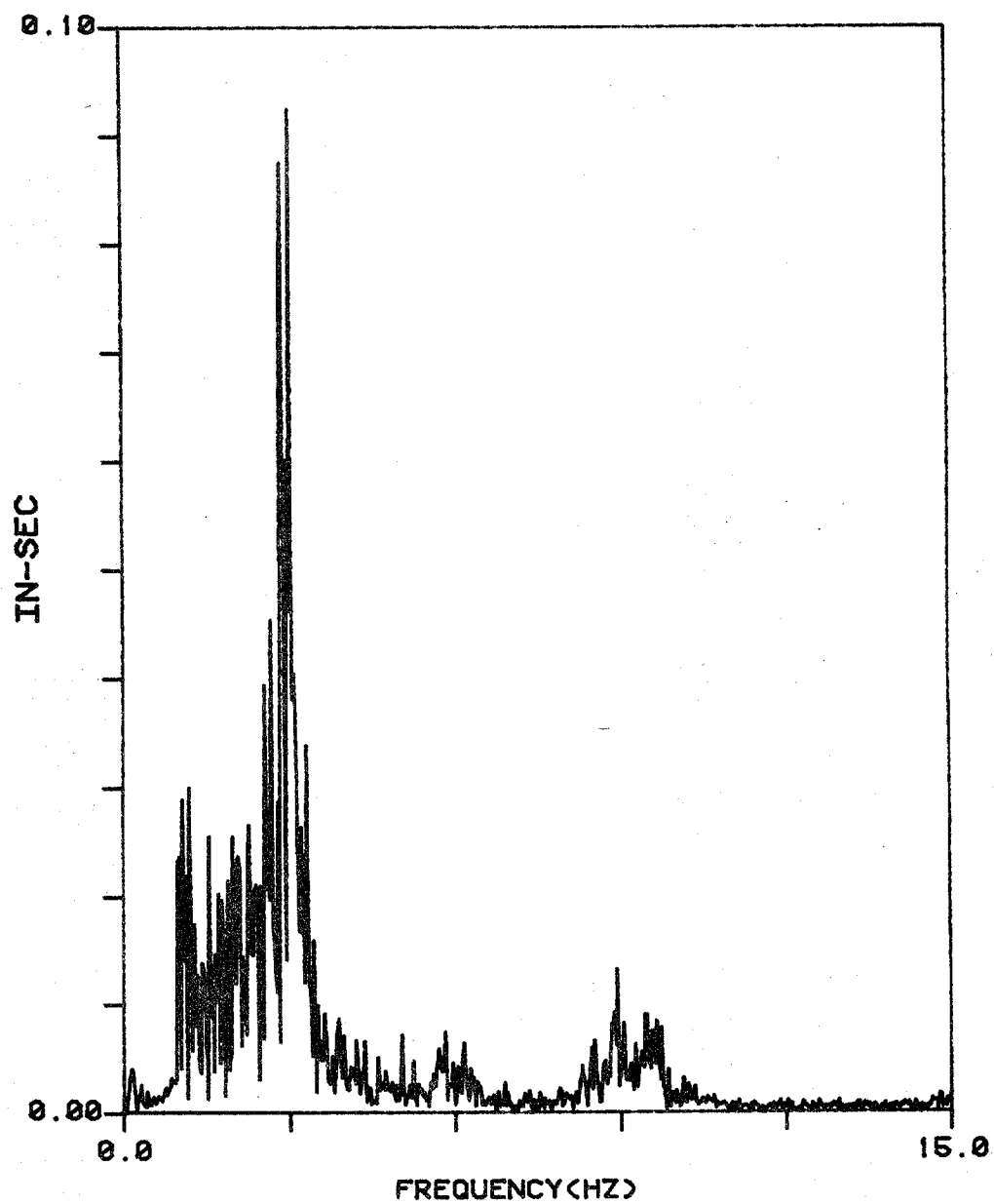


FIGURE 32. FFT OF THE BARE CABLE
DURING NON LOCK-IN RESPONSE.
VERTICAL DISPLACEMENT AT POSITION L/6.

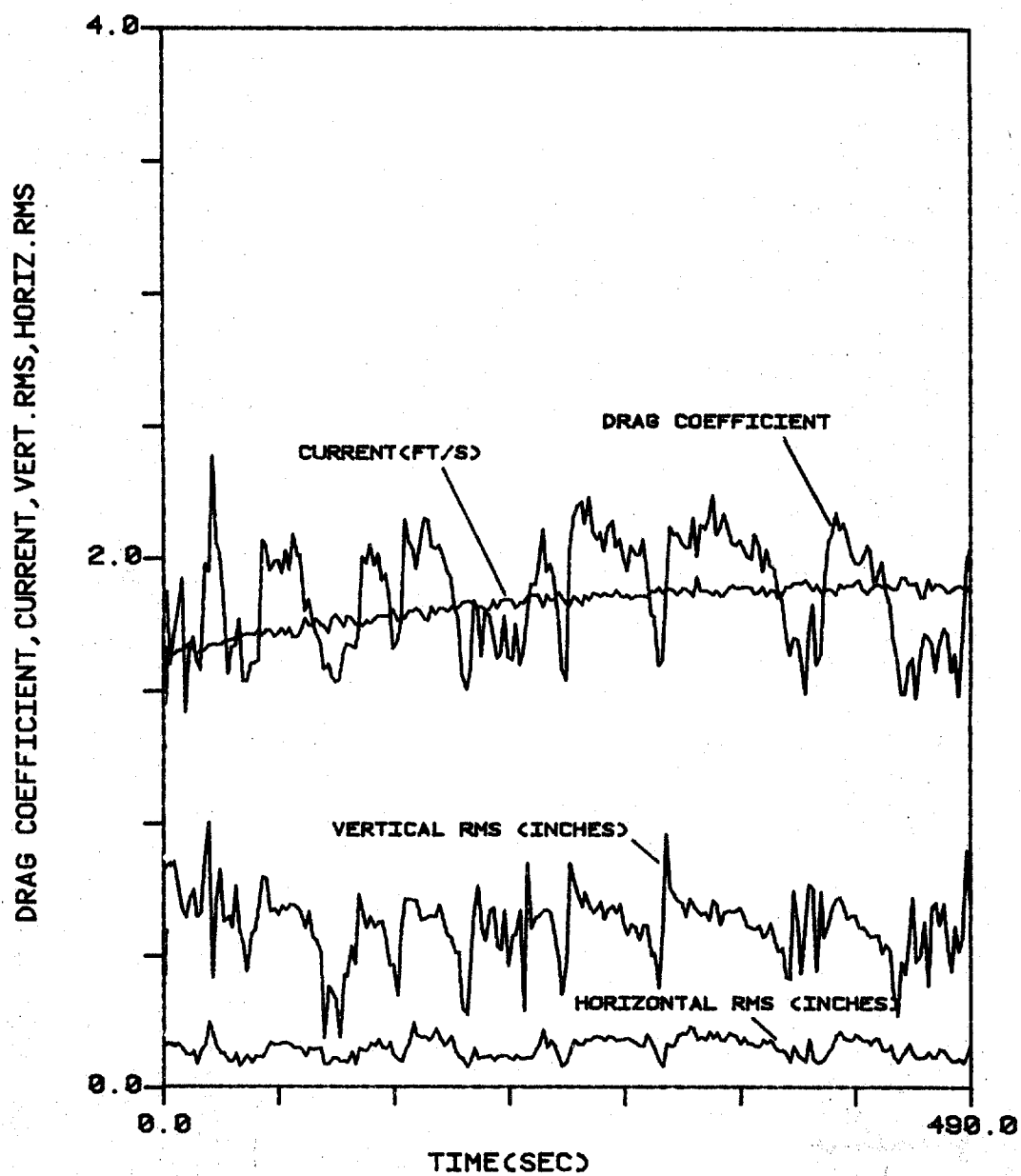


FIGURE 33. STEEL TUBING DURING
NON LOCK-IN RESPONSE.
ACCELEROMETER PAIR AT L/6.

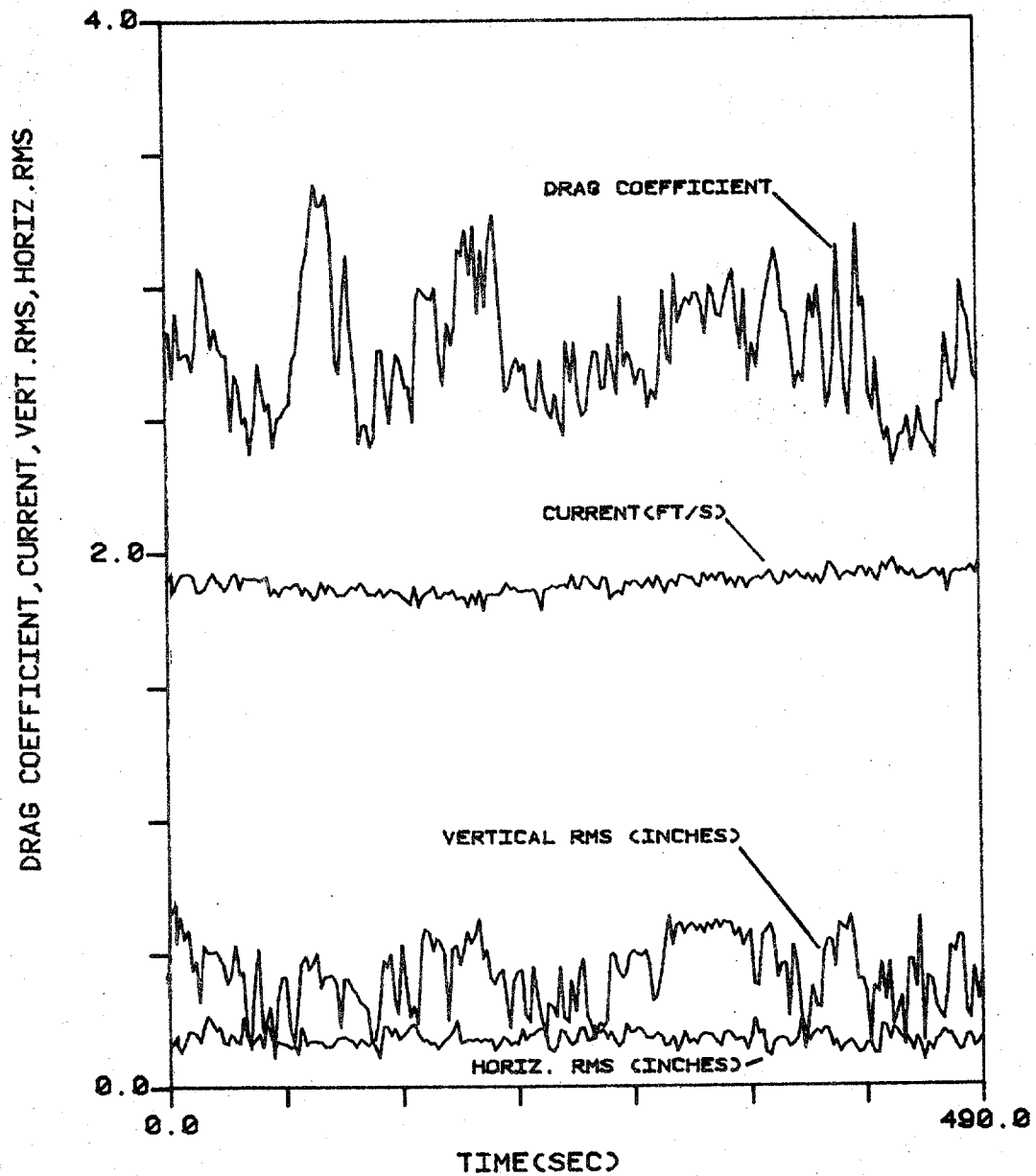


FIGURE 34. BARE CABLE DURING
NON LOCK-IN RESPONSE.
ACCELEROMETER PAIR AT L/6.

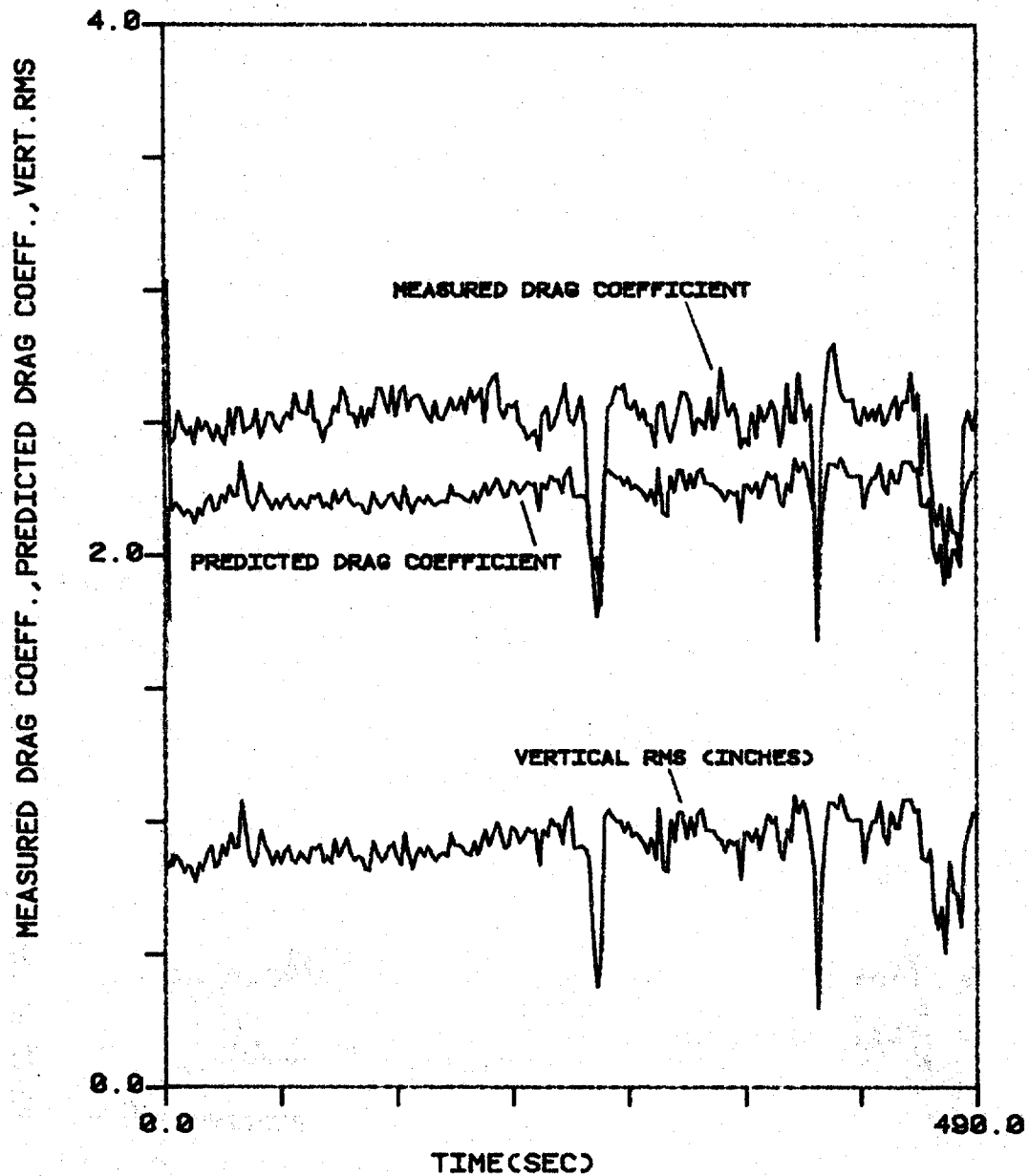


FIGURE 35. PREDICTED DRAG COEFF.
FOR STEEL TUBING DURING THIRD
MODE VERTICAL AND FIFTH MODE HORIZ-
ONTAL RESPONSE. VERTICAL RMS AT L/6.

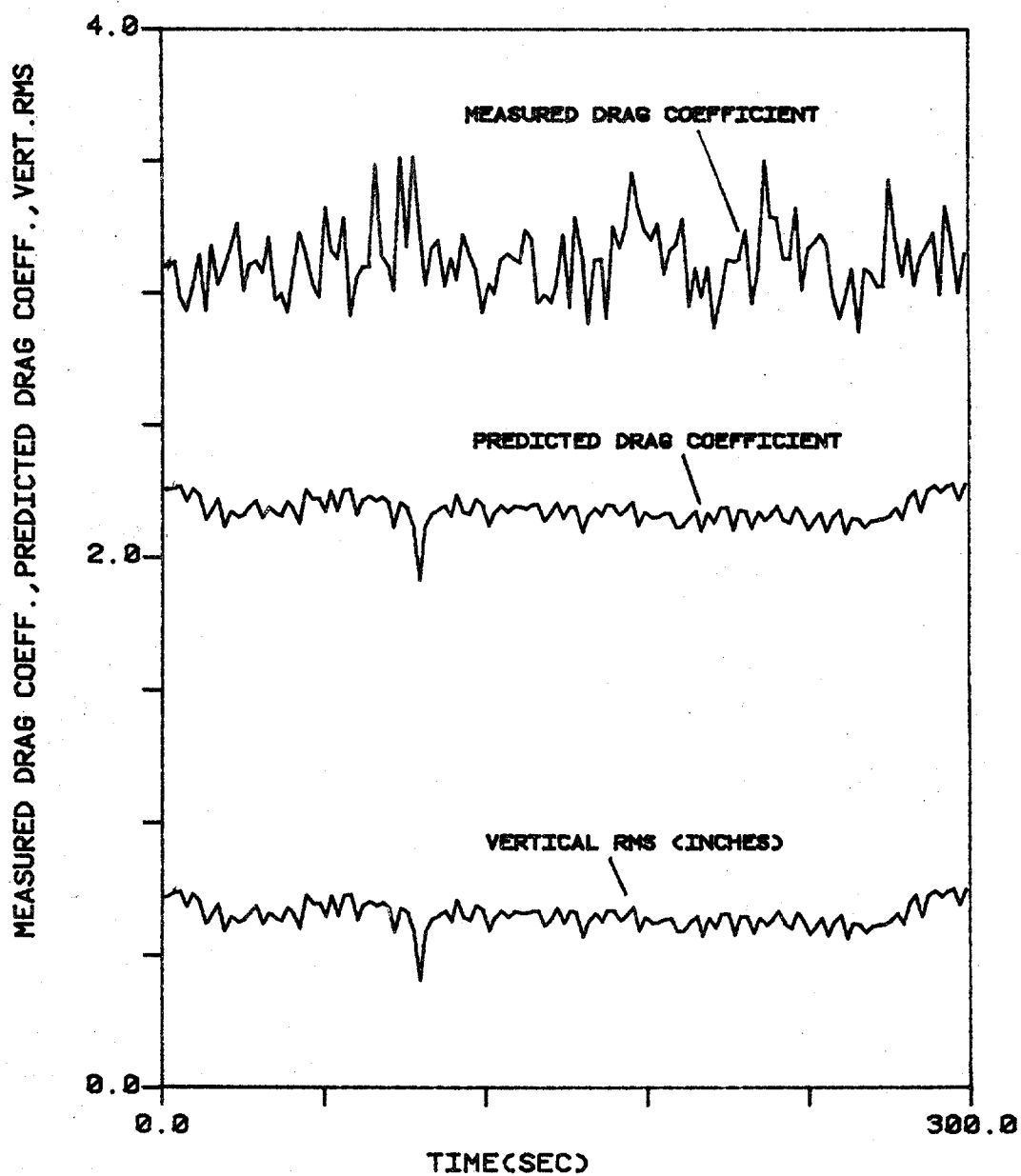


FIGURE 36. PREDICTED DRAG COEFF.
FOR BARE CABLE DURING THIRD
MODE VERTICAL AND FIFTH MODE HORIZ-
ONTAL RESPONSE. VERTICAL RMS AT L/6.

REFERENCES

1. Blevins, R.D., Flow-Induced Vibration, Van Nostrand Reinhold Company, New York, 1977.
2. Blevins, R.D., Formulas for Natural Frequency and Mode Shape, Van Nostrand Reinhold Company, New York, 1979.
3. Dale, J.R., McCandless, J.M. and Holler, R.A., "Water Drag Effects of Flow Induced Cable Vibrations", 68-WA/FE-47, American Society of Mechanical Engineers, Dec. 1968.
4. Every, M.J. King, R. and Griffin, O.M., "Hydrodynamic Loads on Flexible Marine Structures Due to Vortex Shedding," 81-WA/FE-24, American Society of Mechanical Engineers, November 1981.
5. Griffin, O.M., "OTEC Cold Water Pipe Design for Problems Caused by Vortex-Excited Oscillations, Ocean Engineering, Vol. 8, pp. 129-208.
6. Griffin, O.M., "Vortex Excited Unsteady Forces on Resonantly Vibrating, Bluff Structures", NRL Memorandum Report 3820, 1978.
7. Griffin, O.M. and Ramberg, S.E., "On Vortex Strength and Drag in Bluff-Body Wakes", J. Fluid Mech., Vol. 69, part 4, pp. 721-728, 1975.
8. Hallam, M.G., Heaf, N.J. and Wootton, L.R., "Dynamics of Marine Structures: Methods of calculating the dynamic response of fixed structures subject to wave and current action.", Construction Industry Research and Information Association (CIRIA) Report UR 8, 1977.
9. Kan, I., "Cable Strumming Experiments", Society of Naval Architects and Marine Engineers, New England Section, Sept. 26, 1975.
10. King, R., "A Review of Vortex Shedding Research and Its Application", Ocean Engineering, Vol. 4, pp. 141-171, 1977.
11. Newman, J.N., Marine Hydrodynamics, MIT Press, Cambridge, Mass., 1977.
12. Pham, T.H., "Performance Evaluation of Various Strumming Suppression Devices", Thesis presented to the Massachusetts Institute of Technology, Cambridge, Mass., in 1977 in partial fulfillment of the requirements for the degree of Masters of Science.

REFERENCES

(continued)

13. Sarpakaya, T., "Transverse Oscillations of a Circular Cylinder in a Uniform Flow, Part I", Technical Report No. NPS-69SL77071-R, 1977, Naval Postgraduate School, Monterey, California.
14. Sarpakaya, T., "Vortex-Induced Oscillations. A Selective Review." ASME Journal of Applied Mechanics, Vol. 46, June 1979, pp. 241-258.
15. Schargel, R.S., "The Drag Coefficient for a Randomly Oscillating Cylinder in a Uniform Flow," Thesis presented to the Massachusetts Institute of Technology, Cambridge, Mass., in partial fulfillment of the requirements for the degree of Masters of Science.
16. Schuessler, H.W. and Ibler, W., "Digital Filters for Integration", European Conference on Circuit Theory and Design, Institute of Electrical Engineers, Conference Publication No. 116, 1974.
17. Skop, R.A., Griffin, O.M. and Ramberg, S.E., "Strumming Predictions for the SEACON II Experimental Mooring," Proc. Offshore Tech. Conf., Houston, Texas OTC 2884, 1977.
18. Vandiver, J.K. and Mazel, C.H., "A Field Study of Vortex-Excited Vibrations of Marine Cables", Offshore Tech. Conf., Houston, Texas, OTC 2491, 1976.
19. Von Karman, Th., "Uber den Mechanismus des Widerstandes den ein Bewegter Korper in einen Flussiskeit Erfahrt", Nachriser Konigl, Gesselschaft, die Wissenssch, zu Gottingen, 1912.

APPENDIX AINTEGRATION OF EQUATION 2.11

The expression for the local drag coefficient of an oscillating cylinder was given in Equation 2.11 as:

$$\frac{C_{Dl}}{C_{DO}} = 1 + 1.16 \left(\frac{2a}{d} \right)^{.65} \quad (A.1)$$

To find the average drag coefficient for a vibrating flexible cylinder, we must replace the local vibration amplitude with the mode shape, integrate over the length of the cylinder, and then divide by the length. Substituting the mode shape of the flexible cylinder into Equation A.1 gives:

$$\frac{C_{DT}}{C_{DO}} = 1 + 1.16 \left[\frac{2A}{d} \sin \left(\frac{n\pi X}{L} \right) \right]^{.65} \quad (A.2)$$

The average drag coefficient for the flexible cylinder is then:

$$C_{DT} = \frac{1}{L} \int_0^L C_{Dl} dx = \frac{C_{DO}}{L} \int_0^L \left[1 + 1.16 \left(\frac{2A}{d} \sin \left(\frac{n\pi X}{L} \right) \right)^{.65} \right] dx \quad (A.3)$$

This expression can be reduced to:

$$C_{DT} = \frac{C_{DO} n}{L} \int_0^{L/n} dx + \frac{L/n}{L} 1.16 \left[\frac{2A}{d} \sin \left(\frac{n\pi X}{L} \right) \right]^{.65} dx \quad (A.4)$$

Integrating the first expression on the right-hand side and making the substitution $Z = \frac{n\pi X}{L}$ into the second leads to:

$$C_{DT} = C_{DO} \left[1 + \frac{1.16}{\pi} \left(\frac{2A}{d} \right)^{.65} \int_0^{\pi} (\sin Z)^{.65} dZ \right] \quad (A.5)$$

The integral expression on the right-hand side can then be integrated numerically using Simpson's rule to give:

$$\int_0^{\pi} (\sin Z)^{.65} dZ = 2.255 \quad (A.6)$$

The expression for the average drag coefficient for a vibrating flexible cylinder with mode shapes satisfying Equation 2.3 is then:

$$C_{DT} = C_{DO} \left[1 + .833 \left(\frac{2A}{d} \right)^{.65} \right] \quad (A.7)$$

APPENDIX BERRORS IN THE DRAG COEFFICIENT CALCULATIONS

The major source of error in the drag coefficient calculations was thought to be attributable to errors in the drag measurements. The current, projected area, and water density are also important parameters, but any error in their values was considered to be comparatively small. There were two sources of error in the measurement of the drag force on the test cylinders. First, the slope of the calibration line for the drag load cell could only be confirmed to within $\pm 5\%$. Second, the pin that connected the test cylinders to the drag measuring device had a small amount of friction in it that was estimated to be equivalent to at most ± 1.0 lbs. of drag. The combination of these two errors provide an upper and lower bound on the calculated drag coefficients. The upper bound is given by:

$$C_{DU} = \frac{(D \times 1.05) + 1.0}{\frac{1}{2} \rho S V^2} \quad (B.1)$$

and the lower bound is:

$$C_{DL} = \frac{(D \times .95) - 1.0}{\frac{1}{2} \rho S V^2} \quad (B.2)$$

The percent error in the drag coefficient is the percent error in the drag force or:

$$\% \text{ Error} = \left(\pm .05 \pm \frac{1.0}{D} \right) \times 100 \quad (B.3)$$

From this relationship, we can see that as the drag force increases the error due to pin friction will become small and the $\pm 5\%$ calibration error will dominate. The pin friction error can become very important as the drag force becomes small. However, for most of the results presented, the drag force was large enough to keep the pin friction error below 5%. The drag force becomes small enough to cause problems when the current velocity dropped below 1.26 ft/s for the pipe tests and 1.43 ft/s for the cable.

Errors in the velocity measurements have been neglected in these calculations. The absolute calibration of the acoustic current meter is better than 1%. However, it only provided information at one point in the flow 2 feet upstream of the cable at a location 12.5 feet from the drag cell. Spatial non-uniformities on the order of $\pm 3\%$ could be responsible for additional errors in the drag coefficient calculations. These errors will vary as the square of the velocity error and hence imply an additional error of perhaps $\pm 6\%$ in C_D .

APPENDIX CMECHANICAL PROPERTIES AND DIMENSIONS OF
TEST CYLINDERS AND LUMPED MASSESCable Specifications:

Length:	$75.0 \pm .1$ feet
Diameter:	1.25 ± 0.02 inches
Weight per foot in air:	0.7704 pounds per foot
Mass per foot:	0.0239 slugs per foot in air
Specific gravity:	1.408

Pipe Specifications:

Length:	75.0 ± 0.02 feet
Outside Diameter:	$1.631 \pm .003$ inches
Inside Diameter:	$1.493 \pm .003$ inches
Weight per foot in air:	1.231 pounds per foot
Weight per foot in air including weight of the internal cable:	2.001 pounds per foot
Weight per foot including cable and trapped water:	2.236 pounds per foot
Specific gravity of pipe with cable and trap- ped water:	2.40
Measured bending stiffness, EI:	$3.106 \times 10^6 \pm .05 \times 10^6$ pound inches ²

Lumped Mass Properties

Materials:	PVC plastic, copper, lead
Length:	12.0 inches
Outside Diameter:	3.5 inches
Inside Diameter:	1.25 inches
Ballast Hole Diameter:	0.625 inches
Weight in air no lead ballast:	4.41 pounds (2.0 kg)
Weight of water trapped in empty ballast holes when submerged in water:	.55 pounds (.25 kg)
Weight with ballast:	9.97 pounds (4.52 kg)

APPENDIX DDRAG COEFFICIENTS FOR CABLES
WITH ATTACHED LUMPED MASSES

Figure 37 is a 2 1/2 hour plot of drag coefficient current and RMS response of the cable with lumped masses. The physical properties of the lumps may be found in Appendix C. This particular test was one of ten different combinations of the number, location, and weight of lumps used. In this particular case, two light weight lumps were located at points equal to 1/8 and 1/2 of the cable length from the tensionmeter end, and heavy weight lumps were located at the 1/3, 5/8, 3/4, and 7/8 points on the cable. The RMS response data for Figure 37 was taken at the 3/4 point, the location of one of the lumps.

On the plot there are several plateaus in RMS response, which correspond to plateaus in drag coefficient. These regions are likely times of single mode lock in response.

This plot is given as an example of the data set on cables with lumped masses. Much data analysis remains to be completed and will be reported on in subsequent theses, papers, and reports.

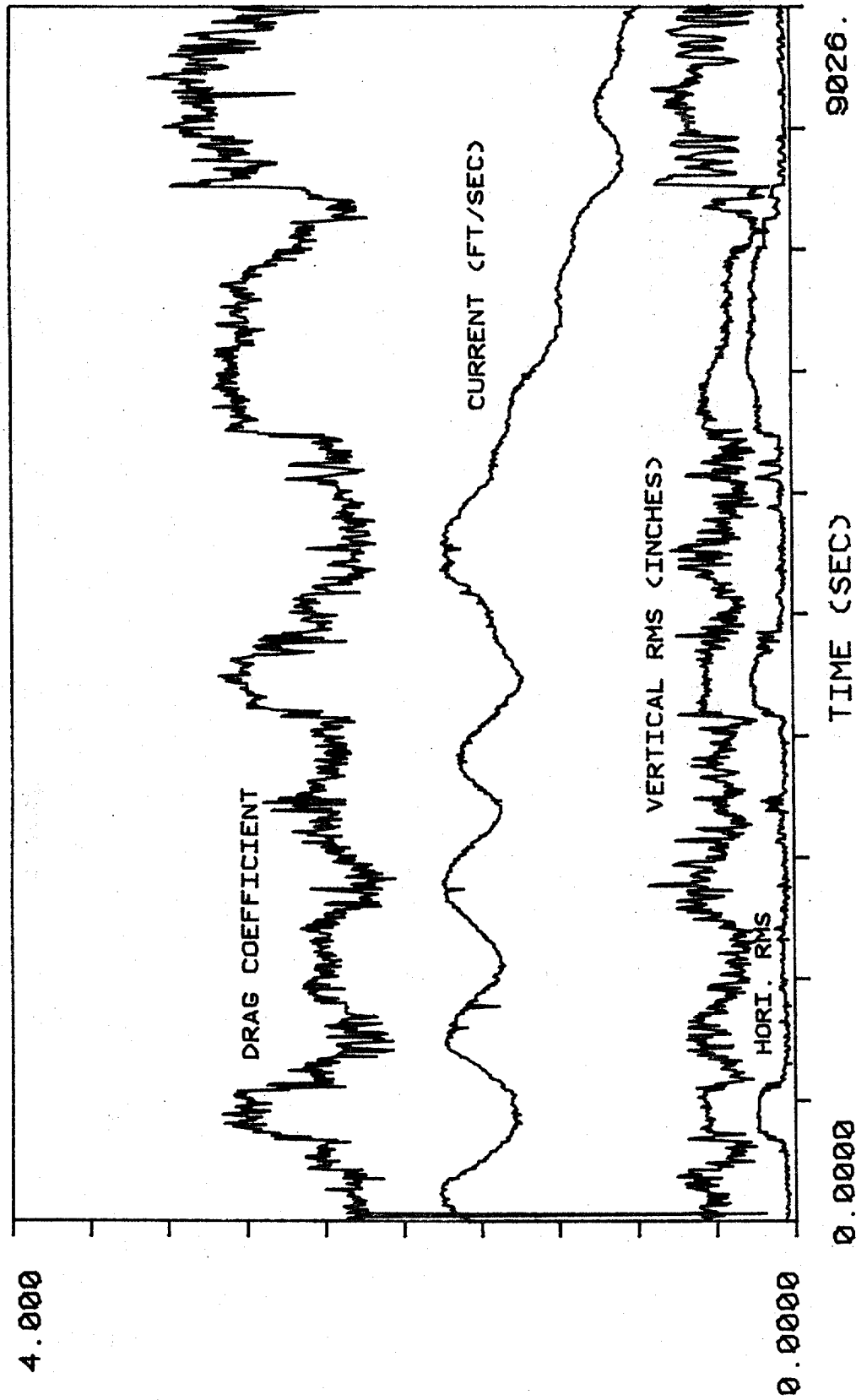


FIG 37. CABLE WITH LUMPED MASSES 10-AUG-81

RMS DATA AT $X=3/4 L$